ACS APPLIED ENERGY MATERIALS

Open Access

This article is licensed under CC-BY 4.0

www.acsaem.org

Article

Regulating Polysulfide Conversion on Fe-N_x Single-Atom Catalysts Supported on Graphitic Carbon Nitride Revealed by Semi-In Situ XPS of Li–S Batteries

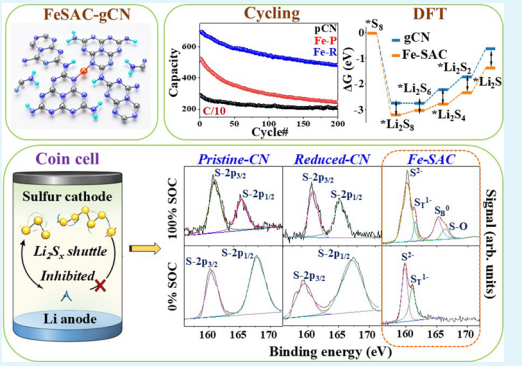
Jyoti Pandey,* Aliakbar Yazdani, Mukesh Singh, Isaac Newton Boakye, Kyle Linford Kilbarger, Carlos Chavez, Zachary Jasper, Benjamin R. Seltin, Adeel Zafar, Bradley D. Fahlman,* Veronica Barone, Mark Wolfman, Chi-Hao Chang, Yi Ding, and Valeri Petkov*

Cite This: https://doi.org/10.1021/acsaem.6c02314

Read Online

ACCESS | Metrics & More | Article Recommendations | Supporting Information

ABSTRACT: Lithium–sulfur batteries are limited by the polysulfide shuttle effect and sluggish conversion kinetics, both strongly influenced by the catalytic interface that mediates the polysulfide redox process. This work centers on the controlled synthesis of single-atom catalysts to establish how the local coordination environment dictates sulfur redox kinetics. We show that engineering the support prior to metal incorporation, rather than the metal site alone, is an effective and reproducible lever for tuning Fe-N_x single-atom catalysis on urea-derived graphitic carbon nitride. Thermal reduction of the support before Fe loading reshapes the resulting Fe-N_x coordination environment, yielding atomically dispersed, coordinatively unsaturated sites with mixed Fe^{2+}/Fe^{3+} valence and no detectable aggregation, as established by X-ray absorption spectroscopy and X-ray photoelectron spectroscopy. Extended X-ray absorption fine structure analysis reveals lower average Fe-N coordination numbers on the reduced support. Density functional theory further demonstrates the catalytic role of atomically dispersed Fe sites by predicting stronger polysulfide adsorption and lower conversion barriers relative to the metal-free gCN support. To resolve how these sites act during operation, we track sulfur speciation across extended cycling using semi-in situ sulfur *2p* X-ray photoelectron spectroscopy, which reveals pronounced enrichment of reduced sulfur species and suppression of oxidized intermediates, direct spectroscopic evidence of accelerated polysulfide conversion. The reduced-support catalysts also show improved durability (~71–75 vs ~48% capacity retention for the bare support). Together, these results establish thermal reduction as a controllable design principle for single-atom catalysts in lithium–sulfur batteries and semi-in situ X-ray photoelectron spectroscopy as a powerful probe of sulfur redox mechanisms.



KEYWORDS: *lithium–sulfur batteries, single-atom catalysts, graphitic carbon nitride, polysulfide conversion, shuttle effect, energy storage, X-ray absorption spectroscopy, semi-in situ XPS*

1. INTRODUCTION

The rapid proliferation of portable electronics, electric vehicles, and grid-scale energy storage has intensified global demand for electrochemical systems that deliver high energy density alongside long-term cycling stability.[1,2] Lithium–sulfur (Li–S) batteries have emerged as one of the most compelling candidates for next-generation energy storage, owing to the high theoretical capacity (1675 mAh g^{-1}) and energy density (~2600 Wh kg^{-1}) of sulfur, combined with its natural abundance, low cost, and low environmental impact.[3,4] Unlike intercalation-based lithium-ion batteries, Li–S cells rely on multielectron conversion reactions, enabling substantially higher theoretical energy densities.[5,6] Despite these intrinsic advantages, the practical realization of Li–S batteries is severely impeded by the well-known polysulfide shuttle effect, the dissolution of soluble lithium polysulfide intermediates in the electrolytes (Li_2S_x, $2 \leq x \leq 8$) that triggers progressive active-material loss, diminished coulombic efficiency, and rapid capacity decay.[7,8] Simultaneously, sluggish polysulfide conversion kinetics, particularly the rate-limiting solid-solid transition from Li_2S_2 to Li_2S, limit sulfur utilization and impede reversibility during extended cycling.[9]

Extensive efforts have been directed toward engineering sulfur host materials capable of simultaneously immobilizing and

Received: July 16, 2026
Revised: September 25, 2026
Accepted: September 28, 2026

Downloaded from pubs.acs.org/aaemcq/article-pdf/doi/10.1021/acsaem.6c02314/68937037/ae-2026-02314j.pdf by CENTRAL MICHIGAN UNIV user on 22 October 2026

© XXXX The Author(s). Published by American Chemical Society

converting polysulfide intermediates.[10,11] Metal-containing electrocatalysts, including transition metals, alloys, and metal compounds, have been intensively investigated as polysulfide regulators, owing to their strong chemical affinity for sulfur species and their ability to accelerate redox kinetics.[12,13] However, high metal loadings introduce a significant electrochemically inactive mass that diminishes practical gravimetric energy density and constrains scalable deployment.[14] Carbon-based hosts offer high electrical conductivity, tunable porosity, and structural robustness as lightweight alternatives,[15,16] but their intrinsically nonpolar character yields only weak interactions with polar polysulfide species. Heteroatom doping and surface functionalization can improve polysulfide adsorption. However, without concurrent catalytic functionality, excessive binding leads to polysulfide accumulation and sluggish conversion kinetics.[17,18] An effective sulfur host must therefore not only immobilize polysulfides but also actively catalyze their reversible electrochemical conversion, a dual requirement that demands precise active-site engineering.[19]

Single-atom catalysts (SACs) have recently emerged as a transformative platform for satisfying this dual requirement, owing to their maximized atomic utilization, well-defined coordination environments, and electronically tunable active sites.[20−22] Among transition metals, iron is particularly attractive for Li–S applications owing to its plentiful natural abundance, rich redox chemistry, and strong affinity for sulfur species. Critically, the preference for Fe over other transition metals (Co, Ni, Mn) is rooted in its electronic structure. Partially filled *d*-orbitals of Fe centers, especially under low-coordination conditions, promote stronger *d*-*p* orbital hybridization with sulfur intermediates and more favorable charge transfer compared to fully coordinated or passivation-prone analogues such as Ni-N_4.[23] Recent studies have demonstrated that coordinatively unsaturated Fe-N_x motifs exhibit superior catalytic activity toward polysulfide conversion, as the low coordination symmetry induces strong charge polarization and enhanced orbital hybridization with sulfur intermediates.[24−27] Stabilizing such coordinatively unsaturated Fe single atoms at high loading without aggregation, however, remains a persistent synthetic challenge that requires a carefully chosen support framework.[28]

Graphitic carbon nitride (gCN) represents a particularly compelling support for Fe-based SACs. Its intrinsically nitrogen-rich framework furnishes abundant pyridinic coordination sites that strongly anchor isolated Fe atoms, suppress aggregation, and enable tunable metal–support interactions.[29,30] Importantly, the physicochemical properties of gCN, including its degree of condensation, defect density, and nitrogen coordination environments, are highly sensitive to precursor chemistry and thermal treatment conditions, providing a versatile handle for modulating the local electronic structure of supported Fe centers.[31] Several recent studies have leveraged this tunability to engineer Fe-N_x sites on gCN for Li–S batteries. Qiu et al. engineered unsaturated Fe-N_2 sites to strengthen lithium polysulfide (LiPS) anchoring and accelerate conversion kinetics.[24] Lu et al. exploited strong N coordination to achieve high single-atom Fe loading under lean-electrolyte conditions,[25] and Ding et al. constructed a bio-templated 3D Fe single-atom/carbon nitride framework with open transport pathways to enhance catalytic site accessibility.[26] These studies collectively establish gCN as a highly effective scaffold for Fe single-atom catalysis in Li–S systems. However, a critical gap persists: the systematic study of support-level modification, specifically thermal reduction of the gCN support, on the local coordination environment of Fe-N_x sites and its downstream consequence on polysulfide conversion. Unlike previously studied systems that use as-synthesized pristine supports, thermal reduction induces changes in defect density, nitrogen speciation, and hydrogen content that are expected to alter Fe-N_x coordination geometry and electronic structure in ways that directly govern catalytic activity.

Equally important is the limitation of conventional characterization approaches in Li–S research. Most mechanistic understanding of polysulfide conversion has relied on ex situ X-ray photoelectron spectroscopy (XPS), synchrotron-based operando X-ray absorption spectroscopy, or in situ Raman spectroscopy, each with inherent constraints in accessibility, surface sensitivity, or ability to capture the chemical state of electrode-bound sulfur species at defined cycling stages.[32] Semi-in situ XPS, in which the electrode is transferred under an inert atmosphere and analyzed at defined states of charge without full atmospheric exposure, offers a practical and surface-sensitive complement to these methods. It directly probes the chemical speciation of sulfur at the cathode surface with high surface sensitivity, avoids the artifacts of ambient exposure, and does not require synchrotron access. As documented in a comprehensive recent review of in situ and operando monitoring tools for Li–S batteries, XPS-based approaches are among the most powerful techniques for resolving the chemical states of sulfur and metal centers during cycling, yet their application to Fe SAC-gCN cathodes under controlled semi-in situ conditions has not been reported.[32] This represents both a methodological and scientific gap that the present work directly addresses.

Herein, we report Fe-N_x single-atom catalysts supported on urea-derived gCN, both pristine (u_pCN) and thermally reduced (u_rCN), as sulfur hosts in Li–S batteries. By systematically varying the support, we tune the local coordination environment and electronic structure of Fe-N_x sites and correlate these changes with polysulfide conversion behavior and electrochemical performance. A comprehensive multitechnique characterization framework, encompassing Fe 2*p* XPS, Fe K-edge X-ray absorption near-edge structure (XANES)/extended X-ray absorption fine structure (EXAFS), magnetization measurements, and DFT calculations, is employed to confirm atomic dispersion, quantify coordination environments, and elucidate the catalytic mechanism. Crucially, semi-in situ S 2*p* XPS is used to directly monitor the evolution of sulfur species during electrochemical cycling across 200 cycles, providing mechanistic evidence that is inaccessible through conventional ex situ analyses. To the best of our knowledge, this is the first study to systematically correlate thermal reduction of the gCN support with Fe-N_x coordination tuning and its impact on polysulfide conversion in Li–S batteries, and the first to apply semi-in situ S 2*p* XPS to this class of Fe SAC-gCN cathode materials to establish a mechanistic picture of polysulfide conversion in Fe-N_x/gCN cathodes. This work thereby establishes a clear structure–property–mechanism relationship and demonstrates semi-in situ XPS as a powerful and broadly applicable diagnostic tool for probing sulfur redox in catalytically functionalized Li–S systems.

Downloaded from pubs.acs.org/aaemcq/article-pdf/doi/10.1021/acsaem.6c02314/6893037/ae-2026-02314j.pdf by CENTRAL MICHIGAN UNIV user on 22 October 2026

https://doi.org/10.1021/acsaem.6c02314
ACS Appl. Energy Mater. XXXX, XXX, XXX−XXX

2. METHODOLOGY

2.1. Synthesis of Pristine Graphitic Carbon Nitride (u_pCN)

Pristine graphitic carbon nitride (u_pCN) was synthesized via thermal condensation of urea as the sole nitrogen-rich precursor. In a typical synthesis, 20 g of urea (99%, Fisher Scientific) was placed in a covered alumina crucible (100 mL) and heated in a muffle furnace at 550 °C for 4 h under an ambient atmosphere at a heating rate of 2.5 °C min^{-1}. The covered crucible was allowed to cool naturally to room temperature inside the furnace, affording approximately 4 g of u_pCN as a yellowish powder, which was collected without further purification.

2.2. Thermally Reduced Graphitic Carbon Nitride (u_rCN)

Thermally reduced graphitic carbon nitride (u_rCN) was obtained by subjecting u_pCN to a secondary heat treatment under dynamic vacuum. In a typical procedure, 6 g of u_pCN was placed in a tube furnace and heated to 590 °C at a ramp rate of 3 °C min^{-1}, then maintained at this temperature for 4 h under a continuous dynamic vacuum of $\sim 10^{-3}$ mbar. The furnace was subsequently allowed to cool naturally to room temperature under the same vacuum conditions, affording approximately 5.3 g of u_rCN (88% yield) as a darker yellow powder relative to the pale yellow u_pCN starting material. The resulting powder was collected and designated as u_rCN. The dynamic vacuum serves two purposes. First, continuous removal of volatile products (H_2O, NH_3, and CO/CO_2 evolved from surface functionalities) shifts the condensation equilibrium forward at a temperature where it would otherwise stall under static conditions. Second, the absence of oxygen permits treatment above the original 550 °C condensation temperature without the oxidative degradation of the framework that occurs in air at comparable temperatures. The treatment is therefore selective in the sense that labile adsorbed species and terminal functional groups are removed while the condensed melon backbone is retained, as confirmed by the preservation of the characteristic (100) and (002) reflections in the XRD pattern of u_rCN (Figure S1c). Throughout this work, "thermal reduction" denotes this post-synthetic vacuum thermal treatment, which results in partial dehydrogenation and deoxygenation of the support, rather than a formal reduction in the redox sense. The resulting structural and electronic modifications are characterized in Section 3.1.

2.3. Synthesis of Fe Single-Atom Catalysts on gCN Supports [Fe-P (Fe Deposited on u_pCN)and Fe-R (Fe Deposited on u_rCN) Series]

Fe single-atom catalysts were deposited onto u_pCN and u_rCN supports via a sonication-assisted wet impregnation method. In a typical procedure, the appropriate mass of iron(III) nitrate nonahydrate ($Fe(NO_3)_3{\cdot}9H_2O$, 98.2%, Fisher Scientific) was dissolved in 100 mL of distilled water under magnetic stirring (180 rpm, 5 min), followed by the addition of 0.92 g of gCN support. The mixture was sonicated (bath sonicator, 40 kHz, room temperature) for 3 h. The resulting suspension was centrifuged at 6300 rpm for 5 min per cycle and washed four to five times with distilled water until the supernatant remained colorless. The solid was dried in a vacuum oven at 55 °C overnight. The powder samples were collected and used as provided. Synthesis parameters for all four samples [labeled as Fe-P1 and Fe-P2 (for Fe deposited on u_pCN) and Fe-R1 and Fe-R2 (for Fe deposited on u_rCN)] are summarized in Table S1.

2.4. Synthesis of Carbon–Sulfur Composites

Carbon–sulfur (C–S) composites were prepared using u_pCN, u_rCN, Fe-P1, Fe-P2, Fe-R1, and Fe-R2 as sulfur hosts. Each gCN host was homogeneously mixed with analytical-grade precipitated sulfur (≥99.99%, Alfa Aesar) at a mass ratio of 75 wt % sulfur to 25 wt % gCN host using an agate mortar and pestle. The mixture was transferred into a Teflon-lined hydrothermal reactor and heated at 155 °C for 12 h to facilitate sulfur infiltration into the porous structure of the carbon host via melt-infusion. The resulting C–S composites were allowed to cool naturally to room temperature and stored under an inert atmosphere to prevent sulfur oxidation and moisture uptake until further use.

2.5. Electrochemical Measurements

All electrolyte preparations and the coin-cell assembly were conducted in an argon-filled glovebox with O_2 and H_2O concentrations maintained below 1 ppm. The electrolyte was prepared by dissolving 2.87 g of lithium bis(trifluoromethanesulfonyl)imide (LiTFSI, anhydrous, ≥99%, SynQuest Laboratories) in 10 mL of a 1:1 (v/v) mixture of 1,2-dimethoxyethane (DME, anhydrous, ≥99%, Sigma-Aldrich) and 1,3-dioxolane (DOL, anhydrous, ≥99%, Sigma-Aldrich). Lithium nitrate ($LiNO_3$, anhydrous, ≥99%, Sigma-Aldrich) was added at 2 wt % as an electrolyte additive to stabilize the lithium metal anode. The solution was stirred overnight to ensure complete dissolution of all components.

Cathodes were prepared by a slurry-casting method. The cathode slurry consisted of the C–S composite as the active material, carbon black (Timcal Super C65, MTI Corp), and poly(vinylidene fluoride) binder (PVDF, grade HSV900, Kynar) in a weight ratio of 7:2:1, dispersed in N-methyl-2-pyrrolidinone (NMP, anhydrous, ≥99%, Sigma-Aldrich). The slurry was homogenized by ball milling in a 20 mL ZrO_2 grinding bowl with 8 ZrO_2 balls at 900 rpm for 30 min. The homogeneous slurry was cast onto an aluminum current collector (15 μm thickness) using an automatic electrode casting machine at an initial wet thickness of 100 μm. The coated electrodes were pre-dried on the casting bed at 70 °C for 15 min, followed by overnight vacuum drying at 50 °C. The dried electrodes were punched into circular disks (diameter = 16 mm) using a precision punch. Active material mass and areal sulfur loading (1.9–2.2 mg cm^{-2}) were determined gravimetrically using a Mettler-Toledo microbalance.

CR2032-type coin cells (stainless steel, MTI Corp) were assembled inside the glovebox using the punched cathode disks, a lithium metal anode (thickness = 0.6 mm, diameter = 16 mm, MTI Corporation), a microporous polypropylene separator (Celgard, USA), and 80 μL of the prepared electrolyte dispensed using an autopipette to maintain a consistent sulfur-to-electrolyte ratio across all cells. The electrolyte-to-sulfur ratio in this study is approximately 18–21 μL mg^{-1}. Although this value is slightly higher than average, it remains consistent with electrolyte loadings commonly employed in small-scale, laboratory-based Li–S studies, where the emphasis is placed on mechanistic evaluation rather than electrolyte minimization. In the CR2032 coin cell configuration, a portion of the electrolyte is associated with separator saturation and interfacial wetting within the confined cell architecture. In addition, the use of a high-surface-area graphitic carbon nitride host combined with atomically dispersed Fe-N_x catalytic sites increases the electrochemically accessible interfacial area, requiring sufficient electrolyte to maintain uniform ionic transport and effective interaction of polysulfide species with active sites. These conditions were therefore intentionally selected to ensure stable electrochemical operation and to enable a clear assessment of the intrinsic catalytic effect on polysulfide conversion. The fabricated cells were galvanostatically cycled at various C-rates within a voltage window of 1.7–2.8 V vs Li/Li^+ using a Maccor Series 4600A battery tester. Specific capacities were calculated based on the mass of active sulfur in the cathode. All C-rates were defined relative to the theoretical capacity of sulfur (1C = 1675 mAh g^{-1}), corresponding to the complete two-electron reduction of elemental sulfur to Li_2S. Cyclic voltammetry (CV) measurements were conducted using coin cells assembled in the same configuration as described above. Prior to CV testing, the cells underwent one formation cycle at C/20 to ensure proper electrode wetting and stabilization of electrochemical interfaces. The measurements were performed in a two-electrode configuration over a voltage window of 1.6–3.0 V vs Li/Li^+ at a scan rate of 0.2 mV s^{-1}. Each cell was subjected to four consecutive cycles. All CV measurements were carried out using a VersaSTAT MC potentiostat (Princeton Applied Research).

Downloaded from pubs.acs.org/aaemcq/article-pdf/doi/10.1021/acsaem.6c02314/6893037/ae-2026-02314j.pdf by CENTRAL MICHIGAN UNIV user on 22 October 2026

https://doi.org/10.1021/acsaem.6c02314
ACS Appl. Energy Mater. XXXX, XXX, XXX–XXX

Electrochemical impedance spectroscopy (EIS) measurements were carried out on CR2032 coin cells using a VersaSTAT 3 over a frequency range of 1 MHz to 1 Hz with an applied AC perturbation amplitude of 10 mV (RMS). The measurements were conducted under open-circuit conditions to evaluate the interfacial and charge-transfer characteristics of the lithium–sulfur battery cells.

2.6. Material Characterization

Powder X-ray diffraction (PXRD) patterns of the samples were recorded using a Rigaku diffractometer operated at 45 kV and 250 mA over the 2θ range of 10–50°. Raman spectra were collected with a Horiba Jobin Yvon Xplora Raman Spectrometer using a 100x microscope objective and a 532 nm excitation of an Nd/YAG laser with a maximum power of 15 mW. The measurements were performed with a 10 mm pinhole and a spectral resolution of 1 cm^{-1}. The laser spot size was 2 mm and the collected data were analyzed with LabVIEW 6 software provided by Horiba in order to precisely locate the Raman bands.

X-ray photoelectron spectroscopy (XPS) measurements were performed on a Kratos Axis Supra + spectrometer equipped with monochromatic Al Kα radiation (1486.6 eV). All core-level spectra were charge-referenced by setting the adventitious C 1*s* peak to 284.8 eV. Peak fitting of the acquired spectra was carried out using XPSPEAK 4.1 software. Semi-in situ S 2*p* XPS measurements were conducted on cathode electrodes retrieved from coin cells at defined states of charge (100% states of charge (SOC) before cycling and 0% SOC after 200 cycles). Electrodes were disassembled inside an argon-filled glovebox, rinsed gently with DME to remove residual electrolyte, and transferred to the XPS instrument under inert conditions to minimize atmospheric exposure.

Magnetization measurements were performed on powder samples of the Fe-loaded gCN materials using a physical property measuring system (PPMS) from Quantum Design. Samples were loaded into polypropylene sample holders, individually mounted onto brass half-tube assemblies, and positioned within the linear transport motor with calibration for maximum signal intensity. Field-dependent magnetization (M-H) measurements were conducted at both 5 K and 300 K. For low-temperature measurements, samples were zero-field cooled (ZFC) from room temperature to 5 K at a controlled rate of 12 K min^{-1}. Once thermal equilibrium was established at 5 K, magnetization data were collected as a function of applied magnetic field swept between +90,000 Oe and –90,000 Oe (+9 T). Following completion of the 5 K measurement, samples were ZFC-warmed to 300 K at the same rate of 12 K min^{-1}, and M-H data were likewise recorded over the same field range. All magnetization data were normalized to the corresponding sample mass and are reported as mass-specific magnetization (emu g^{-1}) as a function of applied field, enabling direct comparison across samples of differing Fe contents.

Elemental analysis of C, H, N, and O content was performed by combustion analysis (Thermo Flash 2000, Alfa Chemistry Testing Lab). Iron content was quantified by inductively coupled plasma optical emission spectrometry (ICP-OES) using an Agilent ICP-OES 730 instrument at the same facility. Detection limits were 100 ppm for combustion analysis and 1 ppm for ICP-OES, consistent with the values reported in Table 1.

X-ray absorption spectra at the Fe K-edge were taken at the 20-BM-B beamline of the Advanced Photon Source at Argonne National Lab. A Si(111) double crystal monochromator was used. The Fe deposited on different carbon nitride supports was measured in fluorescence mode. The raw XAFS spectra were analyzed utilizing the Athena and Artemis interfaces of the Demeter software package.[33] The k^2-weighted EXAFS oscillation in the range 3–14 $Å^{-1}$ was Fourier-transformed, and curve-fitting analysis was performed in the range 0–4 Å in R space. The amplitude reduction factor was estimated by fitting the spectrum of the Fe foil with the parameters calculated with FEFF-6.[34,35] Fits were performed in R-space over a k-range of 3.000–10.939 $Å^{-1}$ with k-weighting of 2, an R-range of 1.0–4.0 Å, and an amplitude reduction factor S_0^2 fixed at 0.9. The curve-fitting analysis was performed considering the crystal structures of the models developed from DFT.

Table 1. Elemental Composition (Atomic Ratios) of Pristine (u_pCN) and Thermally Reduced Graphitic (u_rCN) Carbon Nitride Supports and Their Corresponding Fe-Loaded Samples[a]

sample	composition (atomic unit)
u_pCN	$C_{2.00}N_{2.98}H_{1.19}O_{0.45}$
Fe-P1	$C_{2.00}N_{3.03}Fe_{0.0282}H_{1.23}O_{0.12}$
Fe-P2	$C_{2.00}N_{3.74}Fe_{0.3502}H_{2.70}O_{1.91}$
u_rCN	$C_{2.00}N_{2.96}H_{0.95}O_{0.13}$
Fe-R1	$C_{2.00}N_{2.97}Fe_{0.0845}H_{1.18}O_{0.12}$
Fe-R2	$C_{2.00}N_{3.12}Fe_{0.1399}H_{1.56}O_{0.78}$

[a]C, H, O, and N were analyzed using an organic elemental analyzer (detection limit: 100 ppm), and Fe content was determined by inductively coupled plasma (ICP) analysis (detection limit: 1 ppm).

Morphological characterization was performed using a Hitachi SU3400N-II scanning electron microscope (SEM) equipped with a tungsten filament electron gun and a motorized specimen stage. Transmission electron microscopy (TEM) images were collected using a Hitachi HT7700 TEM with a LaB_6 emitter for a brighter beam to confirm the absence of Fe nanoparticles or clusters and to assess the morphology of the gCN nanosheets.

2.7. Computational Methods and Models

Density functional theory (DFT) calculations were performed using the Vienna Ab initio Simulation Package based on the projector augmented-wave (PAW) method.[36–38] These calculations were employed to evaluate structural properties, adsorption energetics, and to elucidate sulfur reaction behavior on the experimentally relevant supports. All geometry optimizations and adsorption energy calculations were carried out using the Perdew–Burke-Ernzerhof (PBE) exchange–correlation functional, supplemented with Grimme's D3 dispersion correction to account for long-range van der Waals interactions.[39] A plane-wave energy cutoff of 500 eV was applied. The convergence criteria were set to 10^{-6} eV for electronic energy and 0.01 eV $Å^{-1}$ for ionic forces. To eliminate spurious interlayer interactions, a vacuum spacing of 20 Å was introduced along the surface normal. Brillouin zone sampling was performed using a Γ-centered k-point mesh with a grid density of 0.03 $Å^{-1}$, generated via VASPKIT.[40] The decomposition energy barriers of Li_2S were calculated using the climbing image nudged elastic band (CI-NEB) method.[41,42]

3. RESULTS AND DISCUSSION

3.1. Formation and Stabilization of Atomically Dispersed Fe-N_x Sites

The structural integrity and phase identity of both gCN supports and their Fe-loaded counterparts were confirmed by PXRD and Raman spectroscopy (Figure S1 a–d). Both u_pCN and u_rCN exhibit the two characteristic reflections of the melon-like gCN framework, the (100) in-plane peak at ∼13°, and the (002) interlayer stacking peak at ∼27°, confirming that the melon-like structure is preserved after thermal reduction.[31] A slight broadening of the (002) reflection in u_rCN indicates reduced interlayer ordering upon thermal reduction. Raman spectra of both supports show the characteristic D (∼1350 cm^{-1}) and G (∼1580 cm^{-1}) bands, with u_rCN exhibiting a higher D/G ratio than u_pCN (0.94 for u_pCN and 1.01 for u_rCN), reflecting the increased defect density introduced by the thermal reduction process. The Fe-loaded samples retain the

Downloaded from pubs.acs.org/aaemcq/article-pdf/doi/10.1021/acsaem.6c02314/6893037/ae-2026-02314j.pdf by CENTRAL MICHIGAN UNIV user on 22 October 2026

https://doi.org/10.1021/acsaem.6c02314
ACS Appl. Energy Mater. XXXX, XXX, XXX–XXX

same structural signatures. Their PXRD patterns are essentially indistinguishable from those of the parent supports, with no additional reflections attributable to metallic Fe, iron oxides, or other crystalline Fe-containing phases at either loading level, confirming that no bulk crystalline Fe phase is formed. The D and G bands are likewise retained in all Fe-loaded samples, with D/G ratios of 0.91 and 0.89 for Fe-P1 and Fe-P2 and 0.97 and 0.92 for Fe-R1 and Fe-R2. The reduced-support series maintains a consistently higher D/G ratio than the pristine series at every Fe loading, and the modest decrease observed upon Fe incorporation is consistent with partial coordination of Fe at defect and edge nitrogen sites. SEM images confirm the typical wrinkled morphology of urea-derived gCN in all supports and Fe-loaded samples, with no significant morphological changes upon thermal reduction or Fe incorporation and no observable particulate features (Figure S1 e–j).

The chemical changes accompanying vacuum thermal treatment are quantified by elemental analysis (Table 1). The nitrogen-to-carbon ratio is essentially unchanged between u_pCN ($N_{2.98}$) and u_rCN ($N_{2.96}$), confirming that the nitrogen framework is preserved. In contrast, the hydrogen content decreases by approximately 20% (from $H_{1.19}$ to $H_{0.95}$) and the oxygen content by approximately 71% (from $O_{0.45}$ to $O_{0.13}$). The magnitude of the oxygen loss exceeds that attributable to desorption of physisorbed water alone, which would require a proportionally larger hydrogen loss than is observed, indicating genuine elimination of surface oxygen functionalities. Together with the decreased N3 (amino/defect nitrogen) contribution in the N *1s* spectra (Table S3) and the increased Raman D/G ratio, these data establish that the treatment removes terminal -NH_2/-NH groups and surface oxygen species and promotes further condensation, while leaving the melon framework and nanosheet morphology intact.[31] These compositional changes have direct electronic consequences. Terminal amino and surface oxygen functionalities are electron-donating and passivate framework edge sites. Their removal exposes under-coordinated pyridinic nitrogen with greater available lone-pair density and reduces the density of insulating surface groups, improving charge delocalization across the conjugated network. This is reflected experimentally in the electrochemical behavior of the bare supports, where u_rCN exhibits higher redox peak current densities and lower polarization than u_pCN in the absence of any Fe (Figure 4), and in the semi-in situ S 2*p* spectra, where u_rCN alone shows a measurable terminal sulfur contribution at 100% SOC while u_pCN does not (Table 3).

Critically, these surface modifications also govern Fe anchoring. In pristine u_pCN, terminal -NH_2 groups and surface oxygen functionalities provide additional donor atoms capable of chelating Fe during aqueous impregnation. Their removal in u_rCN leaves framework pyridinic nitrogen as the dominant anchoring motif, resulting in fewer donor atoms coordinating each Fe center, the structural origin of the reduced first-shell coordination numbers established by EXAFS in Section 3.2.

A central requirement for effective single-atom catalysis is the formation of isolated metal centers with well-defined coordination environments and suppressed aggregation. Here, Fe-N_x single-atom catalysts were synthesized on both pristine (u_pCN) and thermally reduced (u_rCN) gCN supports, and a comprehensive multitechnique characterization approach was employed to confirm atomic dispersion and evaluate the influence of support modification on Fe speciation.

The synthesis strategy is illustrated schematically in Figure 1a, where Fe species are incorporated into the nitrogen-rich gCN framework via sonication-assisted wet impregnation. Elemental composition data summarized in Table 1 confirm the successful incorporation of Fe into all samples. The Fe content scales systematically with the initial precursor loading, increasing from Fe-P1 to Fe-P2 and from Fe-R1 to Fe-R2, consistent with the two Fe:gCN mass ratios employed during synthesis. Notably, the final Fe atomic fractions determined by ICP analysis (Table 1) are considerably lower than the nominal precursor loadings, consistent with the formation of highly dispersed Fe-N_x sites within the support framework rather than bulk Fe deposition. Anchoring proceeds under these mild aqueous conditions because the melon-like framework already presents a high density of pyridinic nitrogen lone pairs within the cavities between heptazine units, allowing Fe^{3+} to undergo direct ligand exchange from its aquo complex onto pre-formed coordination sites; this is in contrast to nitrogen-doped carbons, in which such sites do not pre-exist and high-temperature pyrolysis is required to form the metal-nitrogen bonds.[29,30] Avoiding a high-temperature step also removes a known pathway for thermally driven metal atom mobility and sintering,[28] consistent with the absence of any Fe–Fe scattering contribution in the EXAFS analysis even at higher Fe loadings (Section 3.2). The corresponding compositions expressed in weight percent are provided in Table S2, to facilitate direct comparison with values reported for other single-atom catalysts. The elemental compositions of u_pCN and u_rCN are consistent with the expected stoichiometry of the melon-like gCN framework, confirming that the nitrogen-rich carbon network is preserved in both pristine and thermally reduced supports.[29,31]

The surface composition and nitrogen speciation of the gCN supports and Fe-loaded samples were investigated by XPS survey and core-level spectra (Figures S2 and S3). The C *1s* spectra of all samples were deconvoluted into two components, C1 and C2, corresponding to graphitic carbon and 3-fold trigonal carbon coordinated by nitrogen atoms within the melon-like framework, respectively.[31] The N 1s spectra of all samples, including the bare supports, exhibit three components upon deconvolution: N1, assigned to pyridinic N within the melon-like framework, N2, corresponding to tertiary bridging N, and N3, attributed to amino/defect-related N species arising from incomplete condensation of the framework.[30,31] The presence of N3 in both u_pCN and u_rCN confirms that even after thermal condensation, residual amino/defect nitrogen species persist within the melon-like framework, consistent with the incomplete condensation character at moderate synthesis temperatures.[43] Quantitative deconvolution of the N *1s* spectra (Table S3) shows that thermal reduction decreases the N3 amino/defect contribution from 10.6 to 6.5% of total nitrogen, a relative reduction of approximately 39%, accompanied by an increase in tertiary bridging N2 from 26.6 to 33.4% and a decrease in pyridinic N1 from 62.9% to 60.1%. The accompanying change in the N1/N2 ratio, from 2.36 in u_pCN to 1.80 in u_rCN, indicates genuine restructuring of the nitrogen framework, in which terminal amino groups are removed under dynamic vacuum and condense with adjacent pyridinic nitrogen to form new bridging linkages. This is consistent with the approximately 20% decrease in hydrogen content between the two supports established by elemental analysis (Table 1). Fe incorporation produces a further

Downloaded from pubs.acs.org/aaemcq/article-pdf/doi/10.1021/acsaem.6c02314/68937037/ae-2026-02314j.pdf by CENTRAL MICHIGAN UNIV user on 22 October 2026

https://doi.org/10.1021/acsaem.6c02314
ACS Appl. Energy Mater. XXXX, XXX, XXX–XXX

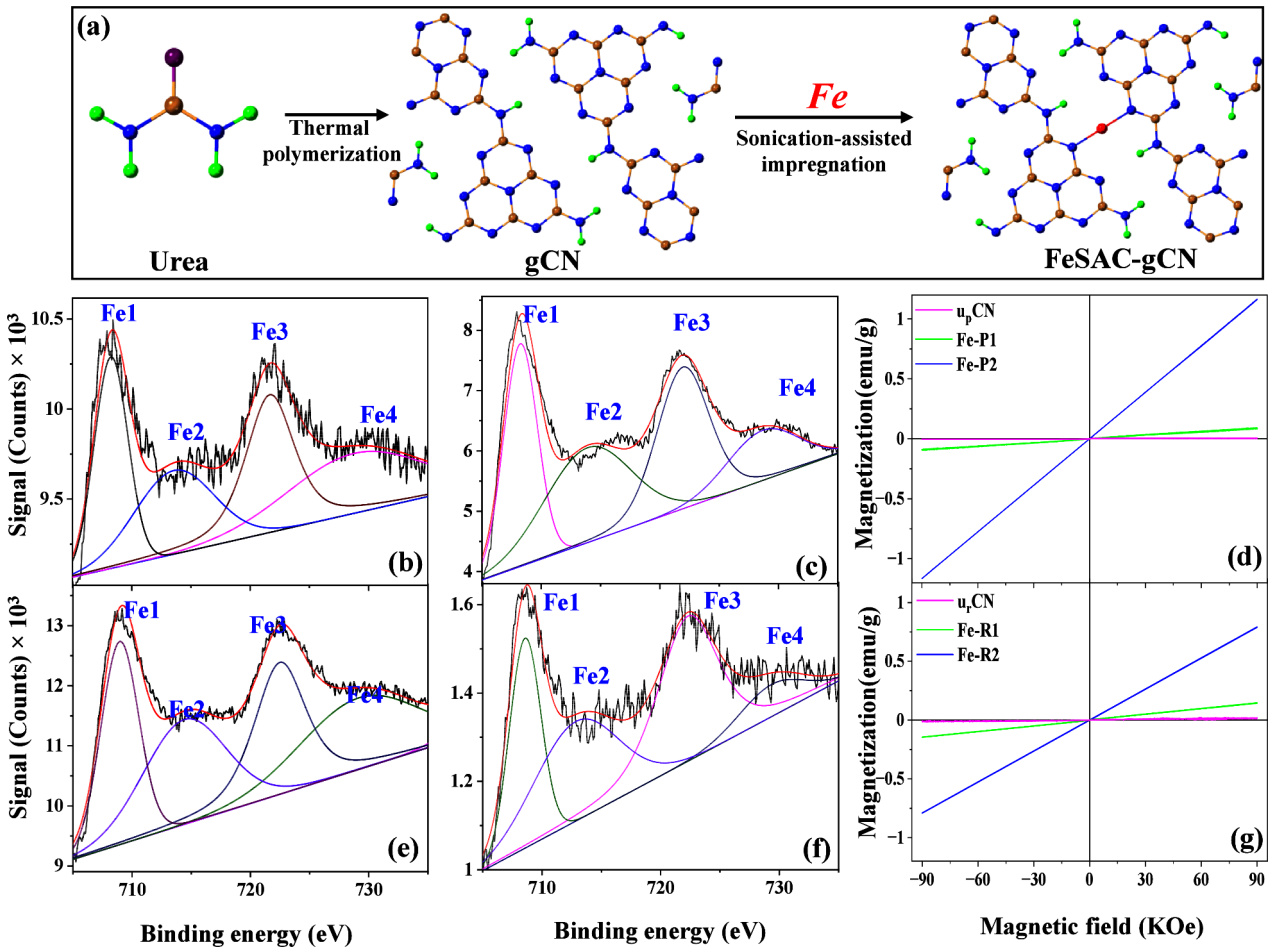


Figure 1. (a) Schematic illustration of the synthesis of Fe single-atom catalysts on graphitic carbon nitride (FeSAC-gCN), where g-C_3N_4 is obtained via thermal polymerization of urea followed by Fe incorporation through sonication-assisted impregnation. C, N, H, O, and Fe are represented in brown, blue, green, magenta, and red, respectively. Core level Fe *2p* XPS spectra with deconvolution for Fe-loaded samples: (b) Fe-P1, (c) Fe-P2, (e) Fe-R1, and (f) Fe-R2, showing multiple fitted components (Fe1-Fe4). The peaks at lower binding energies (~709–712 eV, Fe1 and Fe2) are assigned to the Fe $2p_{3/2}$ signals of Fe^{2+} and Fe^{3+} species coordinated with nitrogen (Fe-N_x), and the component at ~722 eV (Fe3) corresponds to the Fe $2p_{1/2}$ spin-orbit partner, with an observed $2p_{3/2}$–$2p_{1/2}$ splitting of ~13 eV characteristic of Fe species in nitrogen-coordinated environments. The high binding energy feature at ~729–730 eV (Fe4) is attributed to the Fe^{3+} shake-up satellite arising from multiplet splitting and charge-transfer effects. No peak assignable to metallic Fe^0 (~706–707 eV) is detected in any sample, directly ruling out the presence of Fe nanoparticles or metallic clusters. Magnetization (M–H) curves of pristine and Fe-loaded samples: (d) u_pCN, Fe-P1, and Fe-P2, and (g) u_rCN, Fe-R1, and Fe-R2. The linear magnetic response with negligible hysteresis indicates paramagnetic behavior, consistent with atomically dispersed Fe species and no presence of Fe clusters.

systematic depletion of amino/defect nitrogen in both series, with N3 decreasing from 10.6 to 4.3 and 3.9% for Fe-P1 and Fe-P2, and from 6.5 to 3.6 and 3.1% for Fe-R1 and Fe-R2. In both cases, the majority of the decrease occurs at the lower Fe loading, indicating that the accessible amino sites are largely consumed before the higher loading is reached. Notably, the N1/N2 ratio remains within 0.06 of the parent support value for every Fe-loaded sample (2.24 and 2.29 for Fe-P1 and Fe-P2 against 2.36 for u_pCN; 1.86 and 1.79 for Fe-R1 and Fe-R2 against 1.80 for u_rCN), confirming that Fe incorporation consumes terminal nitrogen species without restructuring the framework itself, in agreement with the PXRD and Raman data (Figure S1).

These observations provide a structural basis for the coordination environment established by EXAFS. Terminal amino groups can act as additional donor atoms during aqueous impregnation; their prior depletion in u_rCN therefore leaves the pyridinic nitrogen framework as the dominant anchoring motif, with fewer accessible donors available per Fe center.

The chemical state of the incorporated Fe species was investigated by core-level Fe *2p* XPS (Figure 1). Deconvolution of the spectra yields four components (Fe1–Fe4) for all samples. The peaks at lower binding energies (~709–712 eV, Fe1 and Fe2) are assigned to the Fe $2p_{3/2}$ signals of Fe^{2+} and Fe^{3+} species coordinated with nitrogen (Fe-N_x), consistent with values reported for Fe single-atom systems in nitrogen-coordinated environments.[25,44] The component at ~722 eV (Fe3) corresponds to the Fe $2p_{1/2}$ spin-orbit partner, with an observed $2p_{3/2}$-$2p_{1/2}$ splitting of ~13 eV characteristic of Fe species in nitrogen-coordinated environments. The high binding energy feature at ~729–730 eV (Fe4) is attributed to the Fe^{3+} shake-up satellite arising from multiplet splitting and charge-transfer effects.[45,46] Critically, no peak assignable to metallic Fe^0 (~706–707 eV) is detected in any sample, directly ruling out

https://doi.org/10.1021/acsaem.6c02314
ACS Appl. Energy Mater. XXXX, XXX, XXX–XXX

Downloaded from pubs.acs.org/aaemcq/article-pdf/doi/10.1021/acsaem.6c02314/68937037/ae-2026-02314j.pdf by CENTRAL MICHIGAN UNIV user on 22 October 2026

the presence of Fe nanoparticles or metallic clusters.[47] The coexistence of Fe^{2+} and Fe^{3+} species in all samples reflects the strong electronic interaction between Fe centers and the gCN support, which is known to facilitate charge redistribution within Fe-N_x coordination environments and enhance the catalytic activity.[25] Qualitative comparison of the Fe *2p* spectra between the Fe-P and Fe-R series reveals differences in the relative intensities of the Fe^{2+} and Fe^{3+} components, suggesting that thermal reduction of the support modifies the local electronic environment of the Fe centers, consistent with the coordination number differences established by EXAFS analysis.

Magnetic measurements were also performed alongside XPS measurements to further rule out large clusters (Figure 1). The data indicate that all samples displayed a positive contribution to the susceptibility relative to the diamagnetic susceptibility of the support. A linear response with negligible hysteresis, characteristic of the paramagnetic behavior, also supports the absence of Fe clustering, as expected in Fe single-atom systems. The linearity of this response, even at relatively high fields, is typical of independent and uncoupled interatomic electrons.[48] This meant that the energy of the field appears to compete against the thermal energy of the system rather than any sort of exchange ordering. The difference in susceptibility between samples for both pristine and reduced can be attributed to the concentration of Fe present in the samples. This conclusion is corroborated by TEM analysis (Figure S4), where the absence of observable clusters confirms that Fe species remain isolated from each other, and that the magnetic response arises from Fe-N_x coordination rather than aggregated Fe species. In addition, the magnitude of the magnetic susceptibility scales with the Fe content across both sample series, in agreement with the ICP-derived elemental compositions reported in Table 1. Taken together with the XPS results, the magnetization data provide strong and independent confirmation of atomic Fe dispersion across all samples.

Collectively, the elemental analysis, XPS, magnetization, and TEM data provide a mutually consistent picture of successful Fe incorporation as atomically dispersed Fe-N_x sites across all samples, with thermal reduction of the gCN support introducing systematic modifications to the nitrogen coordination environment. To quantitatively probe the local coordination environment of the Fe-N_x active sites and establish the structural basis for the observed differences between the Fe-P and Fe-R series, Fe K-edge X-ray absorption spectroscopy was performed.

3.2. Coordination Environment and Electronic Structure of Fe-N_x Sites

Having confirmed the atomic dispersion of Fe species across all samples, Fe K-edge XAS measurements were performed to quantitatively probe the local coordination environment and electronic structure of the Fe-N_x active sites. DFT-optimized Fe-N_x structural models embedded in the melon-like gCN framework were used as the starting configuration for individual EXAFS fits (Figure 2b,c,e, and f insets). XAS serves a dual purpose here, as the benchmark technique for unambiguously confirming single-atom dispersion through the absence of metal-metal scattering paths,[49,50] and as the primary tool for quantifying the Fe-N_x coordination environment with bond-distance and coordination-number precision inaccessible to XPS or magnetization measurements alone. Determining whether the thermal reduction of the gCN support alters the Fe-N_x coordination geometry requires this degree of structural resolution.

The normalized XANES spectra of all Fe-loaded samples, compared with reference compounds (Fe foil, FeO, and Fe_2O_3), are shown in Figure 2. The absorption edge positions of all Fe-P and Fe-R samples lie between those of FeO and Fe_2O_3, confirming that Fe exists in a partially oxidized, nonmetallic state with mixed Fe^{2+}/Fe^{3+} character, in full agreement with the aforementioned Fe 2p XPS results. The spectra are clearly distinct from the Fe foil reference, providing unambiguous confirmation that no metallic Fe^0 is present in any sample. A notable pre-edge feature is observed in all samples (Figure 2a and d insets), arising from the formally dipole-forbidden *1s* to *3d* electronic transition. The presence and intensity of this feature are characteristic of distorted, low-symmetry coordination geometries deviating from centrosymmetry, as expected for coordinatively unsaturated Fe-N_x single-atom sites where the local environment breaks inversion symmetry.[49,51]

The Fourier-transformed EXAFS spectra in R-space for individual Fe-loaded samples are presented in Figure 2 (phase-corrected), with overlaid and stacked comparisons against reference compounds shown in Figure S5. All four Fe-loaded samples display a dominant peak at approximately 1.98–1.99 Å (Table 2) attributed to first-shell Fe-N (peak I) scattering,[51,52] consistent with Fe-N bond distances reported for Fe single-atom catalysts in nitrogen-coordinated carbon environments.[25] A weaker feature at approximately 3.01–3.08 Å (Table 2) is assigned to second-shell Fe-N/C (peak II) scattering contributions from the surrounding melon-like framework.[52,53] Importantly, no scattering feature attributable to FeFe coordination, clearly visible at ∼2.4 Å in the Fe foil reference (Figure S5), is observed in any of the four samples, providing the most direct and explicit evidence that Fe remains atomically dispersed throughout, even at the higher Fe loading levels used for Fe-P2 and Fe-R2.[52,54] The Fe-N and Fe-O scattering paths cannot be reliably distinguished by EXAFS, as nitrogen and oxygen are adjacent in atomic number with nearly identical backscattering amplitude and phase, and the corresponding bond distances are very close.[49,53] The fitted first-shell distances of 1.987–1.998 Å are nonetheless shorter than the Fe-O distances characteristic of the octahedral oxide references and lie within the range reported for Fe-N coordination in nitrogen-doped carbon frameworks,[23] providing a first indication in favor of Fe-N. More decisively, the presence of bulk iron oxide phases is excluded by the higher-shell behavior: both FeO and Fe_2O_3 exhibit intense Fe-O-Fe scattering in R-space (Figure S5) that is entirely absent in all four samples. This assignment is further supported by the XANES line shapes, which differ from both oxide references despite lying between them in the edge position, and by the pronounced pre-edge features observed in all samples (Figure 2a and d insets), inconsistent with the centrosymmetric octahedral coordination of bulk FeO and Fe_2O_3. Together with the Fe *2p* and N *1s* XPS data, the absence of clusters in TEM, and the paramagnetic magnetic response, these observations establish nitrogen coordination within the melon-like framework as the dominant first-shell environment.

Quantitative EXAFS fitting parameters extracted using Artemis are summarized in Table 2. The first-shell Fe-N bond distances are remarkably consistent across all four samples, ranging from 1.987 to 1.998 (Å), in good agreement with Fe-N_x bond lengths reported for Fe single-atom catalysts in nitrogen-coordinated carbon environments.[23,25] The consistency of Fe-N bond distances across all samples indicates that the local Fe-N bonding chemistry is similar in nature regardless

Downloaded from pubs.acs.org/aaemcq/article-pdf/doi/10.1021/acsaem.6c02314/6893037/aae-2026-02314j.pdf by CENTRAL MICHIGAN UNIV user on 22 October 2026

https://doi.org/10.1021/acsaem.6c02314
ACS Appl. Energy Mater. XXXX, XXX, XXX–XXX

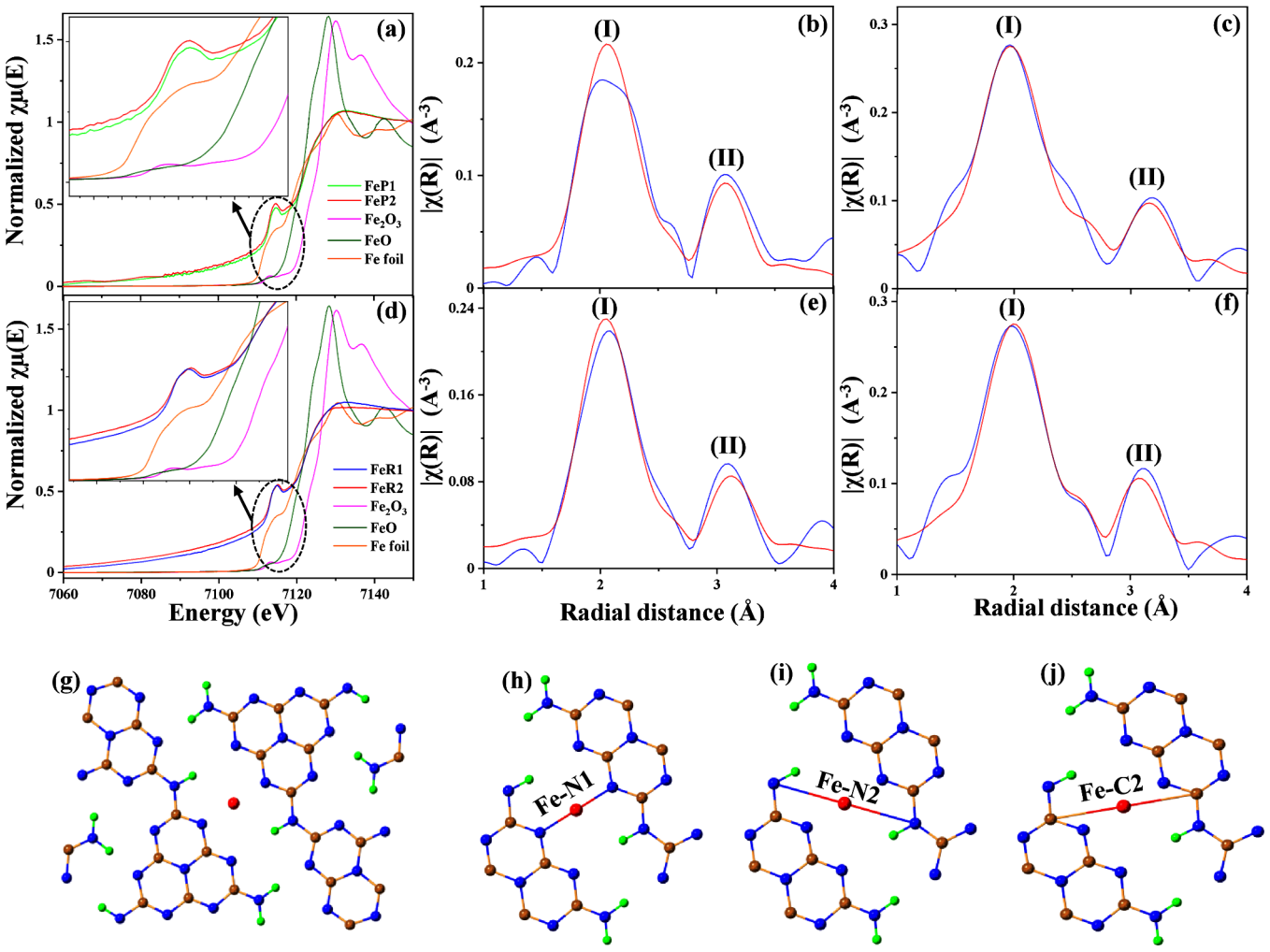


Figure 2. Fe K-edge X-ray absorption spectroscopy analysis of Fe-loaded gCN samples. (a and d) Normalized XANES spectra of Fe-P and Fe-R samples compared with reference compounds (Fe foil, FeO, and Fe_2O_3). Insets highlight the pre-edge region, indicating variations in Fe oxidation state and local coordination environment. (b, c, e, and f) Phase-corrected Fourier transform EXAFS spectra in R-space for Fe-P1, Fe-P2, Fe-R1, and Fe-R2, respectively, with corresponding fits. Spectra are phase-corrected using the Fe-N scattering path, such that the dominant peak (I) at approximately 1.99 Å corresponds directly to the first-shell Fe-N bond distance reported in Table 2. The weaker feature (II) arises from second-shell scattering contributions (Fe-N/C). The absence of a distinct Fe-Fe scattering feature indicates that Fe remains predominantly atomically dispersed, even at higher loadings and after thermal reduction. (g–j) DFT-optimized structural models used for EXAFS fitting, illustrating representative Fe-N and Fe-C coordination environments. Carbon, nitrogen, hydrogen, and iron atoms are shown in brown, blue, green, and red, respectively.

Table 2. EXAFS Fitting Parameters for Fe-Loaded gCN Samples at the Fe K-Edge[a,b]

sample	bond distance of the 1st shell (Fe-N1)	1st shell average coordination number	1st shell Debye-Waller factor	bond distance of the 2nd shell (Fe-N2/C2)	2nd shell average coordination number	2nd shell Debye-Waller factor	R-factor
Fe-P1	1.988 Å	1.89(45)	0.009(2)	3.058 Å	0.43(23)	0.006(2)	0.0509
Fe-P2	1.990 Å	1.95(39)	0.008(3)	3.089 Å	0.47(21)	0.007(2)	0.0300
Fe-R1	1.987Å	1.12(40)	0.009(1)	3.012 Å	0.498(32)	0.008(3)	0.0462
Fe-R2	1.998 Å	1.38(50)	0.007(2)	3.020 Å	0.525(36)	0.009(1)	0.0282

[a]Bond distances, average coordination numbers, and Debye–Waller factors (σ^2) are reported for the first and second coordination shells, together with the *R*-factor for each fit. [b]The first-shell contribution corresponds to Fe-N/O scattering, assigned to Fe-N on the basis of the combined XANES, XPS, TEM, and magnetization; second-shell contributions are attributed to Fe-N/C paths. Coordination numbers represent ensemble averages over all Fe centers probed and are correlated with the corresponding Debye–Waller factors; a control refinement with σ2 constrained to a common value across all samples preserves the systematic reduction in first-shell coordination number for the Fe-R series.

of support type, and that thermal reduction does not alter the Fe-N bond length significantly. The average first-shell coordination numbers, however, differ markedly between the two-sample series. Fe-P1 and Fe-P2, supported on pristine u_pCN, exhibit coordination numbers of 1.89 and 1.95, respectively, indicating near-two-fold Fe-N coordination. In contrast, Fe-R1

https://doi.org/10.1021/acsaem.6c02314
ACS Appl. Energy Mater. XXXX, XXX, XXX–XXX

Downloaded from pubs.acs.org/aaemcq/article-pdf/doi/10.1021/acsaem.6c02314/68937037/ae-2026-02314j.pdf by CENTRAL MICHIGAN UNIV user on 22 October 2026

and Fe-R2, supported on thermally reduced u_rCN, show significantly lower coordination numbers of 1.12 and 1.38, respectively. While the absolute coordination numbers carry fitting uncertainties typical of EXAFS analysis (Table 2), the systematic trend toward lower coordination in the Fe-R series relative to the Fe-P series is robust and consistent across both Fe loading levels, and is independently corroborated by the N *1s* XPS observations.

It is worth mentioning that EXAFS coordination numbers represent ensemble averages over all Fe centers probed, and the noninteger values obtained here should not be interpreted as a single, uniformly coordinated site geometry. Adopting a minimal two-component description comprising Fe-N_1 and Fe-N_2 motifs, the simplest model supported by the available number of independent data points, the fitted values correspond to approximately 89 and 95% Fe-N_2 in Fe-P1 and Fe-P2 vs approximately 88 and 62% Fe-N_1 in Fe-R1 and Fe-R2. A three-component decomposition, including Fe-N_3 motifs, is not statistically justified at the present data quality and is not attempted. Because coordination number and Debye–Waller factor are correlated in EXAFS analysis, a control refinement was performed in which the first-shell σ^2 was constrained to a common value across all four samples. The systematic reduction in the first-shell coordination number for the Fe-R series relative to the Fe-P series persists under this constraint, while the second-shell parameters remain essentially identical across all samples, confirming that the difference is specific to the first coordination shell. We further note that while the absolute coordination numbers carry a systematic uncertainty arising from the transfer of S_0^2 from the metallic Fe foil reference to nitrogen-coordinated Fe, this offset is common to all four samples, which were measured and analyzed under identical conditions, so the relative comparison is unaffected.

This systematic reduction in coordination number across the entire Fe-R series constitutes direct and quantitative structural evidence that thermal reduction of the gCN support modifies the local Fe-N_x coordination geometry, producing more coordinatively unsaturated Fe centers. This finding is mechanistically consistent with the N *1s* XPS data discussed in the previous section, where thermal reduction was shown to deplete the amino/defect nitrogen population by approximately 39%, while leaving the framework backbone intact. The present study compares two supports and therefore establishes a consistent mechanistic link between nitrogen speciation and Fe coordination, rather than a quantitative correlation across a continuous range of nitrogen speciation. Coordinatively unsaturated Fe-N_x environments of this type are known to induce stronger electronic asymmetry, enhanced charge polarization, and more favorable *d–p* orbital hybridization with sulfur intermediates, properties that translate directly into superior catalytic activity for polysulfide conversion.[24,26,54,55] The second-shell coordination parameters (Fe-N2/C2 at 3.012–3.089 Å, Table 2) are consistent across all samples, indicating that the broader melon-like framework environment is preserved despite the difference in first-shell coordination, further validating that thermal reduction selectively modifies the Fe-anchoring geometry rather than disrupting the support structure. The absence of Fe–Fe coordination is further supported by the fitting analysis itself: satisfactory fits to the R-space data for all four samples were obtained using only Fe-N and Fe-N/C scattering paths, with no Fe–Fe contribution required to reproduce the experimental spectra (Table 2). Given that Fe–Fe scattering produces a strong and readily identifiable feature in the metallic and oxide references (Figure S5), any aggregated Fe species present must constitute a negligible fraction of the total Fe.

Collectively, the XANES and EXAFS analyses, supported by the XPS, magnetization, and TEM data, provide a comprehensive and mutually consistent structural picture. That is, Fe exists predominantly as atomically dispersed Fe-N_x sites with mixed Fe^{2+}/Fe^{3+} valence states across all samples, no Fe aggregation or metallic phases are present, and thermal reduction of the gCN support systematically lowers the average Fe-N coordination number, from ∼1.9 in the Fe-P series to ∼1.1–1.4 in the Fe-R series, by modifying the nitrogen speciation of the melon-like framework. This structural distinction between the Fe-P and Fe-R series is expected to govern the differences in catalytic activity, polysulfide conversion behavior, and electrochemical performance, as established by DFT calculations and semi-in situ XPS in the sections that follow.

3.3. Electrochemical Performance of Fe-N_x/gCN Cathodes

The electrochemical performance of the Fe-N_x/gCN cathodes was evaluated in CR2032 coin cells vs Li/Li^+ within a voltage window of 1.7–2.8 V, using a sulfur loading of 1.9–2.2 mg cm^{-2}. Rate capability, long-term cycling stability, and CV measurements were performed to establish the practical impact of Fe-N_x incorporation and support thermal reduction on polysulfide conversion kinetics and reversibility.

The galvanostatic charge–discharge (GCD) profiles confirm the role of Fe single-atom catalytic sites in improving sulfur redox kinetics. GCD profiles of u_rCN and Fe-R1 cathodes collected at C/20 are presented in Figure 3a, exhibiting the characteristic two-plateau discharge profile associated with the stepwise reduction of elemental sulfur to long-chain lithium polysulfides (upper plateau, ∼2.3 V vs Li/Li^+) and subsequently to insoluble Li_2S_2/Li_2S (lower plateau, ∼2.0 V vs Li/Li^+). Fe-R1 delivers substantially higher discharge capacity at both plateaus relative to u_rCN, directly reflecting the improved sulfur utilization and reduced electrochemical polarization conferred by the coordinatively unsaturated Fe-N_x sites. Closer inspection of the initial charge profiles (Figure 3b) reveals a suppressed charge overpotential in Fe-R1 relative to u_rCN, particularly in the early charging region associated with Li_2S/Li_2S_2 decomposition. The initial charge bump decreases from approximately 2.342 V for u_rCN to 2.258 V for Fe-R1, corresponding to an 84 mV reduction. When defined relative to the stabilized early charge plateau, the initial charge overpotential decreases from approximately 98 mV for u_rCN to 51 mV for Fe-R1. This 47 mV reduction indicates that Fe single-atom sites lower the Li_2S/Li_2S_2 oxidation barrier and facilitate the reverse sulfur redox reaction. This behavior is consistent with the substantially reduced Li_2S decomposition barrier (1.50 to 0.76 eV) established by DFT calculations discussed below, confirming the catalytic role of Fe-N_x sites in facilitating the rate-limiting charging step. Rate-dependent GCD profiles of Fe-R1 collected across C/20 to 1C (Figure 3c) confirm progressive voltage polarization at higher current densities, with both discharge plateaus shifting as expected for increasing ohmic and kinetic overpotentials. It shows that the cell retains characteristic Li–S charge–discharge behavior as the rate increases from C/20 to 1C, although with the expected increase in polarization and decrease in accessible capacity. When the current density is returned to C/20, the voltage profile and capacity largely recover, indicating good electrochemical reversibility after high-rate operation. The retention of

Downloaded from pubs.acs.org/aaemcq/article-pdf/doi/10.1021/acsaem.6c02314/6893037/ae-2026-02314j.pdf by CENTRAL MICHIGAN UNIV user on 22 October 2026

https://doi.org/10.1021/acsaem.6c02314
ACS Appl. Energy Mater. XXXX, XXX, XXX–XXX

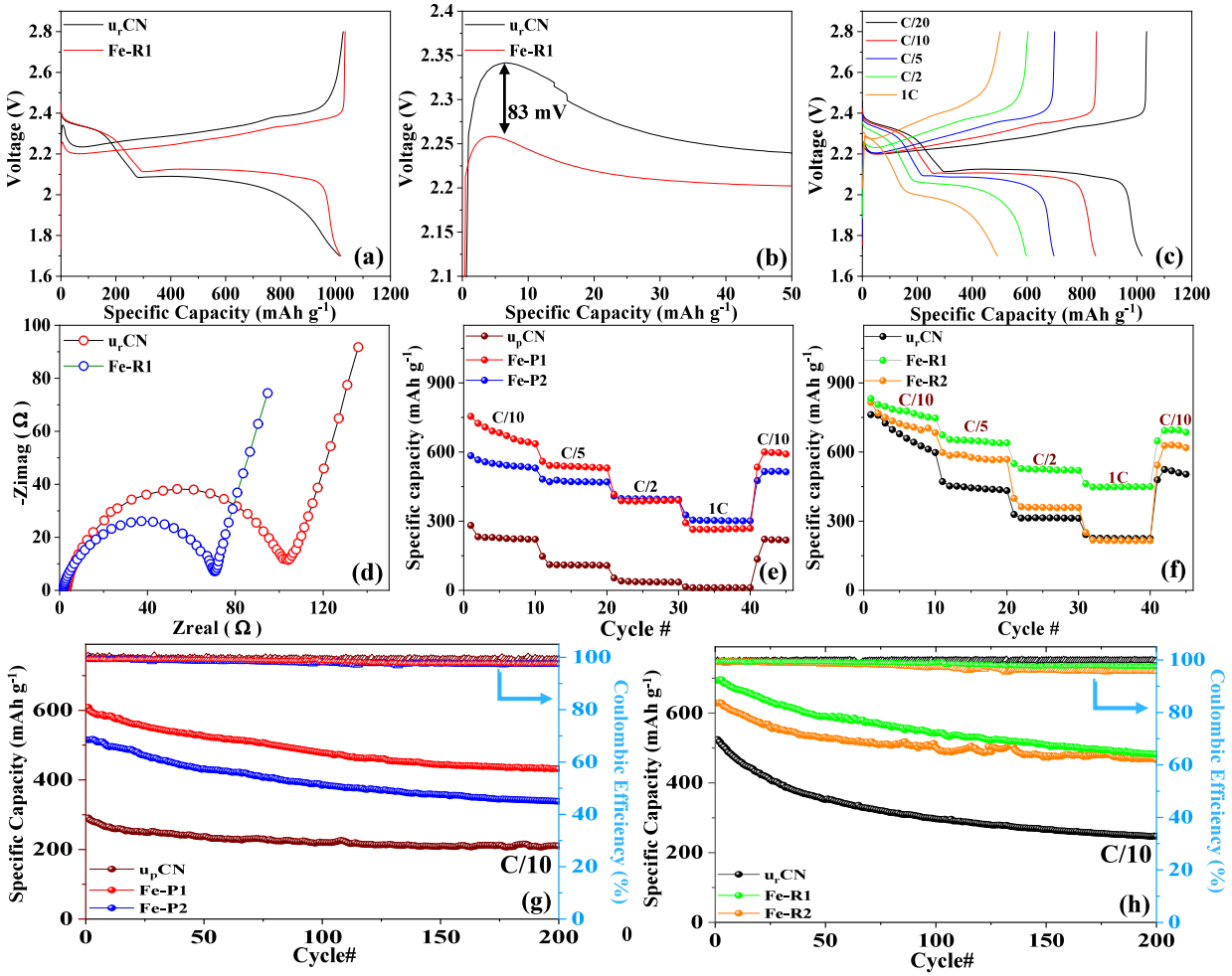


Figure 3. Electrochemical performance comparison of pristine and reduced graphitic carbon nitride-based Li–S cathodes with and without Fe single-atom catalyst incorporation. (a) Galvanostatic charge–discharge (GCD) voltage profiles of the reduced graphitic carbon nitride baseline cathode, u_rCN, and the Fe single-atom catalyst-containing cathode, Fe-R1, collected at C/20. (b) Zoomed-in charge profiles at the beginning of charging for u_rCN and Fe-R1, highlighting the initial charge overpotential associated with Li_2S/Li_2S_2 oxidation. The suppressed initial charge polarization observed for Fe-R1 indicates a reduced Li_2S decomposition barrier and improved catalytic reversibility of the sulfur redox process. (c) Rate-dependent charge–discharge voltage profiles of Fe-R1 collected at different C-rates from C/20 to 1C and subsequently returned to C/20, showing the evolution of voltage polarization and capacity response under increasing current density. (d) Nyquist plots of u_rCN and Fe-R1 obtained by electrochemical impedance spectroscopy, showing reduced interfacial/charge-transfer resistance for the Fe-containing cathode. (e) Rate performance of pristine graphitic carbon nitride-based cathodes, including u_pCN, Fe-P1, and Fe-P2, was measured across sequential current densities from C/10 to 1C and recovered at C/10. (f) Rate performance of reduced graphitic carbon nitride-based cathodes, including u_rCN, Fe-R1, and Fe-R2, was measured under the same rate sequence. (g) Long-term cycling performance and Coulombic efficiency of the pristine graphitic carbon nitride series at C/10. (h) Long-term cycling performance and Coulombic efficiency of the reduced graphitic carbon nitride series at C/10. The Fe-containing cathodes exhibit improved sulfur utilization, reduced charge polarization, lower impedance, enhanced rate capability, and improved cycling stability compared with their corresponding baseline cathodes. The reduced graphitic carbon nitride series shows particularly favorable electrochemical behavior, suggesting that reduction-induced structural/electronic modification of the carbon nitride framework, together with Fe single-atom catalytic sites, promotes polysulfide conversion, facilitates Li_2S/Li_2S_2 formation–decomposition kinetics, and improves Li–S redox reversibility.

two well-resolved discharge plateaus even at 1C attests to the kinetic robustness of the Fe-N_x active sites under fast discharge conditions. Electrochemical impedance spectroscopy further supports improved interfacial kinetics after Fe incorporation. As shown in Figure 3d, Fe-R1 displays a smaller Nyquist semicircle than u_rCN, with the apparent charge-transfer resistance decreasing from approximately 100.9 to 68.9 Ω, a reduction of about 31.8%. The solution/internal resistance also decreases from approximately 3.06 to 1.67 Ω. Although these values are estimated directly from the Nyquist response rather than equivalent-circuit fitting, the trend indicates more favorable charge transfer in Fe-R1, consistent with its lower initial charge polarization and improved Li_2S/Li_2S_2 conversion kinetics.[26]

The rate capabilities of the pristine support series (u_pCN, Fe-P1, and Fe-P2) and the reduced support series (u_rCN, Fe-R1, and Fe-R2) across current densities ranging from C/10 to 1C are presented in Figure 3e,f, respectively. Across all current densities tested, Fe-loaded samples consistently outperform their corresponding bare gCN supports, confirming the catalytic role of the Fe-N_x sites in accelerating polysulfide conversion and reducing kinetic barriers. Within the pristine support series,

https://doi.org/10.1021/acsaem.6c02314
ACS Appl. Energy Mater. XXXX, XXX, XXX–XXX

Downloaded from pubs.acs.org/aaemcq/article-pdf/doi/10.1021/acsaem.6c02314/68937037/ae-2026-02314j.pdf by CENTRAL MICHIGAN UNIV user on 22 October 2026

both Fe-P1 and Fe-P2 deliver markedly higher discharge capacities than bare u_pCN does at each current density (Figure 3e), with Fe-P1 showing the greater improvement of the two. A similar trend is observed within the reduced support series, where Fe-R1 and Fe-R2 substantially exceed the capacity of bare u_rCN at all rates tested (Figure 3f). Noticeably, the Fe-R series consistently outperforms the Fe-P series at all current densities, demonstrating that the coordinatively unsaturated Fe-N_x environments generated by the thermal reduction of the support translate directly into superior rate performance, a finding fully consistent with the lower Fe-N coordination numbers and enhanced electronic asymmetry established by EXAFS analysis.[26,55] Upon returning to C/10 after high-rate cycling, all Fe-loaded samples recover capacities close to their initial values, indicating robust structural integrity of the Fe-N_x active sites under repeated charge–discharge cycling and confirming the stability of the single-atom coordination environment under operating conditions.[26,54] Long-term cycling stability was assessed at C/10 over 200 cycles (Figure 3g and h). Among all samples, Fe-R1 delivers the best overall performance, with an initial discharge capacity of 693.5 mAh g^{-1} and a retained capacity of 490.7 mAh g^{-1} after 200 cycles, corresponding to a capacity retention of ∼71%. Fe-R2 achieves an initial capacity of 629.0 mAh g^{-1} with a retained capacity of 470.6 mAh g^{-1} (∼75% retention) after 200 cycles. In comparison, the bare u_rCN support delivers an initial capacity of 525.1 mAh g^{-1} but retains only 251.3 mAh g^{-1} after 200 cycles (∼48% retention), highlighting the critical role of the Fe-N_x sites in suppressing capacity fade. Within the pristine support series, Fe-P1 achieves an initial capacity of 600.0 mAh g^{-1} with a retained capacity of 397.1 mAh g^{-1} (∼66% retention), while Fe-P2 delivers an initial capacity of 516.3 mAh g^{-1} with a retained capacity of 340.9 mAh g^{-1} (∼66% retention) after 200 cycles. Bare u_pCN delivers an initial capacity of 291 mAh g^{-1}, retaining 216.2 mAh g^{-1} (∼75% retention), though the low absolute retained capacity underscores the limited electrochemical activity of the unmodified support. Across both series, the Fe-loaded samples exhibit markedly superior capacity retention compared to their bare gCN counterparts. The Fe-R series consistently outperforms the Fe-P series in both initial capacity and retention, consistent with the more coordinatively unsaturated Fe-N_x environment established by EXAFS, which is expected to provide stronger adsorption and more efficient catalytic conversion of polysulfide intermediates.[24,55] The capacity retention demonstrated by Fe-R1 and Fe-R2 over 200 cycles, alongside the marked improvement over bare gCN supports, is consistent with the broader trend established for Fe-N_x single-atom cathodes in Li–S batteries, wherein coordinative unsaturation of the Fe center has been identified as a key structural descriptor governing polysulfide adsorption strength and catalytic conversion efficiency.[24,26,54] The corresponding average capacity-fade rates over 200 cycles are 0.146 and 0.126% per cycle for Fe-R1 and Fe-R2, compared with 0.169 and 0.170% per cycle for Fe-P1 and Fe-P2 and 0.261% per cycle for the bare u_rCN support, quantifying the improvement in durability conferred by the Fe-N_x sites.

The electrochemical performance does not scale monotonically with the Fe content. Within both series, the lower-loading sample delivers the higher initial discharge capacity (Fe-P1, 600.0 mAh g^{-1}, vs Fe-P2, 516.3 mAh g^{-1}; Fe-R1, 693.5 mAh g^{-1}, vs Fe-R2, 629.0 mAh g^{-1}), and Fe-P2 delivers the lowest initial capacity of the Fe-loaded series despite carrying the highest total Fe content. This behavior parallels the EXAFS results, in which the average first-shell coordination number increases with Fe loading within each series, indicating that higher Fe occupancy of the available nitrogen anchoring sites produces a progressively more saturated average coordination environment. Taken together, these observations indicate that catalytic performance is governed by the coordination environment of the Fe centers rather than by their absolute concentration.

The experimental design employed here also permits partial deconvolution of support-level and Fe-coordination contributions, since both bare supports were evaluated alongside their Fe-loaded counterparts. Thermal reduction increases the BET surface area of the support from 154 to 188 m^2 g^{-1} and the Raman D/G ratio from 0.94 to 1.01,[31] and correspondingly increases the initial discharge capacity of the bare support from 291.0 to 525.1 mAh g^{-1}. These modifications do not, however, confer durability: bare u_rCN exhibits the lowest capacity retention of any sample examined (47.9%, vs 75% for u_pCN), indicating that increased surface area and defect density improve sulfur accessibility without providing the polysulfide anchoring and catalytic conversion functions necessary for stable cycling. Comparing retained capacities after 200 cycles, support modification alone contributes 35 mAh g^{-1} and Fe incorporation on the pristine support 181 mAh g^{-1}; purely additive behavior would predict 432 mAh g^{-1} for Fe-R1, whereas 490.7 mAh g^{-1} is observed. This supra-additive response indicates that support modification and Fe incorporation are not independent contributions, but that the modified support alters the coordination environment of the Fe sites themselves.

To further contextualize the electrochemical stability of the present Fe-N_x/gCN cathodes, the cycling performance of Fe-R1 and Fe-R2 was compared with representative Fe-N_x single-atom catalysts and other advanced sulfur hosts reported in the literature, as summarized in Table S4 and Figure S6. Although several highly engineered Fe-N_x systems have achieved higher capacity retention, the Fe-R series shows a particularly favorable balance between cycling stability, testing severity, material simplicity, and synthetic accessibility. Fe-R2 retains approximately 75% of its capacity after 200 cycles at C/10, while Fe-R1 retains approximately 71% under the same conditions. This performance is competitive with several advanced catalytic sulfur hosts,[24–26,56–65] including HFeNG-S, which retained 73.8% after 100 cycles at C/10 using a holey Fe, N-doped graphene architecture;[62] Co-N/G, which retained 75% after 200 cycles at C/5 using atomically dispersed Co–N sites in graphene;[60] Fe-N-C/S-MCF, which retained 65.2% after 100 cycles at C/2 using a mesocellular foam carbon host;[63] and Li_2S@NC:SAFe, which retained 75.1% after 200 cycles at 1C using a single-atom Fe-modified nitrogen-doped carbon framework.[64] Importantly, the C/10 cycling condition used here provides a relatively demanding evaluation of polysulfide retention because the longer cycle time allows greater opportunity for soluble polysulfide diffusion and shuttle-related loss than higher-rate tests. Higher retentions have been reported for more intensively engineered systems, including SAFe@g-C_3N_4, which retained 90% after 200 cycles at C/5 under lean-electrolyte conditions;[25] S@3DFeSA-CN, which retained 87.7% after 200 cycles at C/5 using a biotemplated single-atomic Fe-N_2 mediator architecture;[26] and Fe-N_2/CN@S, which retained 90% after 100 cycles at C/5 through precise Fe-N_2 site synthesis.[24] In contrast, the present Fe-N_x/gCN cathodes are prepared through a

Downloaded from pubs.acs.org/aaemcq/article-pdf/doi/10.1021/acsaem.6c02314/68937037/ae-2026-02314j.pdf by CENTRAL MICHIGAN UNIV user on 22 October 2026

https://doi.org/10.1021/acsaem.6c02314
ACS Appl. Energy Mater. XXXX, XXX, XXX–XXX

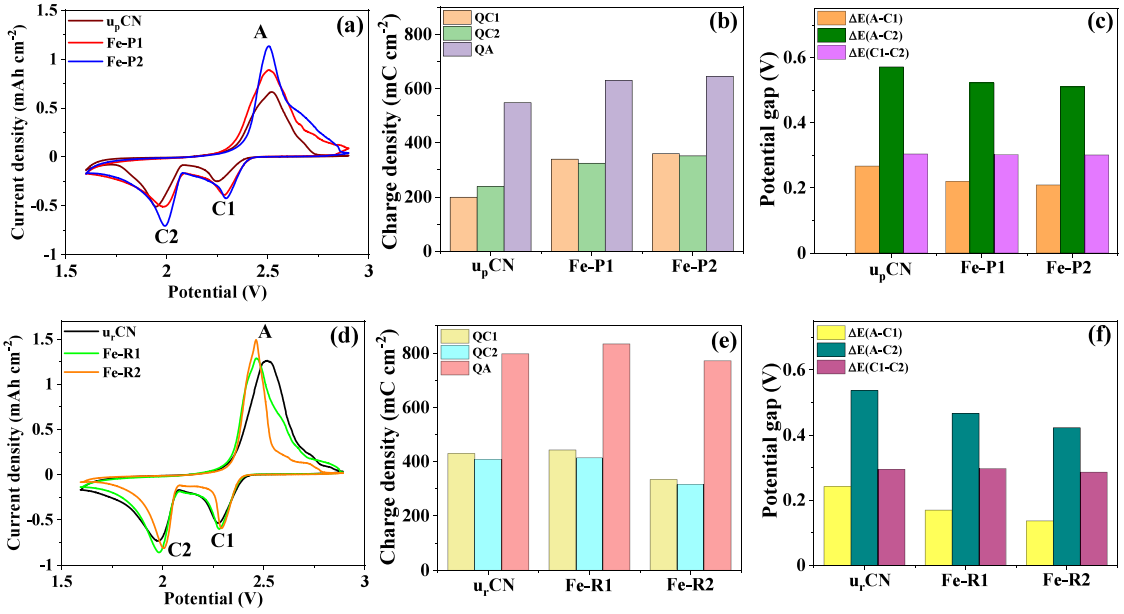


Figure 4. Comparative cyclic voltammetry analysis of Li–S cells prepared using pristine and reduced graphitic carbon nitride-based sulfur cathodes with and without Fe single-atom catalyst. (a) CV profiles of pristine graphitic carbon nitride-based cathodes, including u_pCN, Fe-P1, and Fe-P2, collected at 0.2 mV s^{-1}. (b) Approximate peak-area charge density extracted from the cathodic and anodic redox peaks of the u_pCN-series cathodes. (c) Potential gaps between redox peaks for the u_pCN-series cathodes, including ΔE(A-C1), ΔE(A-C2), and ΔE(C1-C2). (d) CV profiles of reduced graphitic carbon nitride-based cathodes, including u_rCN, Fe-R1, and Fe-R2, collected at 0.2 mV s^{-1}. (e) Approximate peak-area charge density extracted from the cathodic and anodic redox peaks of the Fe-R series cathodes. (f) Potential gaps between redox peaks for the u_rCN series cathodes, including ΔE(A-C1), ΔE(A-C2), and ΔE(C1-C2). The cathodic peaks C1 and C2 correspond to the stepwise reduction of sulfur to soluble long-chain polysulfides and subsequently to insoluble Li_2S_2/Li_2S, respectively, while the anodic peak A corresponds to the reverse oxidation of Li_2S/Li_2S_2 to higher-order polysulfides/sulfur. Incorporation of Fe single-atom catalytic sites increases the redox peak-area charge density and decreases the peak-to-peak polarization, particularly ΔE(A-C2), indicating accelerated Li_2S_2/Li_2S formation–decomposition kinetics and improved sulfur redox reversibility. The graphitic carbon nitride framework may also contribute to polysulfide retention through polar N-rich chemical anchoring sites and structural confinement of soluble polysulfide intermediates. Compared with the pristine graphitic carbon nitride series, the reduced graphitic carbon nitride cathodes show lower polarization gaps and strong anodic charge contribution, suggesting more favorable sulfur redox reversibility.

comparatively simple sonication-assisted wet impregnation of $Fe(NO_3)_3{\cdot}9H_2O$ onto urea-derived graphitic carbon nitride followed by thermal reduction under mild vacuum, without sacrificial templates, MOF-derived intermediates, biotemplates, or additional high-temperature carbonization. This distinction is important because graphitic carbon nitride is intrinsically N-rich and can simultaneously provide polar polysulfide-interacting sites and coordination environments for Fe-N_x formation. Thus, the Fe-R cathodes demonstrate that meaningful improvements in Li–S cycling stability do not require highly elaborate scaffold design; instead, rational modification of an inexpensive, N-rich gCN support can generate catalytically active Fe-N_x environments capable of approaching the performance of more complex single-atom sulfur hosts.

CV profiles of the pristine and reduced support series are shown in Figure 4. All samples exhibit the characteristic two cathodic peaks and one anodic peak associated with the stepwise sulfur redox reactions in Li–S batteries. The first cathodic peak at ∼2.3 V vs Li/Li^+ corresponds to the reduction of elemental sulfur to long-chain lithium polysulfides (Li_2S_x, $4 \le x \le 8$), while the second cathodic peak at ∼1.98 V vs Li/Li^+ is attributed to the further reduction of long-chain polysulfides to short-chain Li_2S_2 and Li_2S.[23] The single anodic peak at ∼2.5 V vs Li/Li^+ corresponds to the reverse oxidation of Li_2S to higher-order polysulfides and ultimately elemental sulfur. Compared to the bare gCN supports, all Fe-loaded samples exhibit sharper and more symmetric redox peaks with reduced peak-to-peak separation, indicating lower electrochemical polarization and faster redox kinetics. This improvement is more pronounced in the Fe-R series relative to the Fe-P series, consistent with the lower coordination number and higher catalytic activity of the Fe-N_x sites in the thermally reduced samples established. The enhanced redox reversibility observed for the Fe-R series is further corroborated by the reduced overpotential between the two cathodic processes, reflecting a more thermodynamically favorable polysulfide conversion pathway facilitated by the coordinatively unsaturated Fe-N_x active sites.[26,55] To quantify the kinetic improvements observed qualitatively in the CV profiles, the peak-area charge densities (QC1, QC2, and QA) and peak-to-peak potential gaps (ΔE) were extracted from the CV data for all samples (Figures 4b,c,e,and f). Since all CV curves were collected at the same scan rate of 0.2 mV s^{-1}, differences in peak current, peak-area charge density, and peak-to-peak potential gap can be used to compare relative redox kinetics and polarization. For the pristine graphitic carbon nitride series (Figure 4a–c), Fe incorporation increases the redox peak response and reduces electrochemical polarization compared with u_pCN. In particular, Fe-P2 increases the current densities of C1, C2, and A from 0.2506, 0.5104, and

Downloaded from pubs.acs.org/aaemcq/article-pdf/doi/10.1021/acsaem.6c02314/68937037/ae-2026-02314j.pdf by CENTRAL MICHIGAN UNIV user on 22 October 2026

https://doi.org/10.1021/acsaem.6c02314
ACS Appl. Energy Mater. XXXX, XXX, XXX–XXX

0.6644 mA cm^{-2} for u_pCN to 0.4251, 0.7076, and 1.1336 mA cm^{-2}, respectively. The A-C2 peak separation [ΔE(A-C2)], which reflects the polarization between Li_2S_2/Li_2S formation and its reverse oxidation, also decreases from 0.5714 V for u_pCN to 0.5226 V for Fe-P1 and 0.5104 V for Fe-P2. This decrease indicates reduced polarization for the Li_2S_2/Li_2S formation–decomposition process. The reduced graphitic carbon nitride series (Figure 4d–f) shows stronger overall electrochemical activity and lower polarization than the pristine series. u_rCN already exhibits higher peak current densities and redox charge contributions than u_pCN, suggesting that reduction of the carbon nitride framework improves electrochemical accessibility and sulfur redox kinetics. Fe incorporation further enhances this effect: the A-C2 peak separation [ΔE(A-C2)] decreases from 0.5370 V for u_rCN to 0.4668 V for Fe-R1 and 0.4226 V for Fe-R2, corresponding to reductions of approximately 13.1 and 21.3%, respectively. The decrease in the A–C1 peak separation [ΔE(A-C1)] , which reflects the polarization between soluble polysulfide formation and reverse oxidation, also suggests improved reversibility involving soluble polysulfide redox processes. Overall, the CV results indicate that Fe single-atom catalytic sites promote sulfur redox conversion and reduce electrochemical polarization in both pristine and reduced graphitic carbon nitride hosts. The reduced carbon nitride framework provides a more favorable electrochemical environment, likely through improved electronic/structural accessibility and stronger interaction with polysulfide intermediates.

Collectively, the electrochemical results demonstrate that Fe-N_x incorporation onto the gCN support significantly enhances capacity, rate performance, and cycling stability relative to bare gCN, and that the thermally reduced Fe-R series consistently outperforms the pristine Fe-P series across all electrochemical metrics. These observations are directly consistent with the structural picture discussed above: the more coordinatively unsaturated Fe-N_x sites in the Fe-R series provide stronger polysulfide anchoring and more efficient catalytic conversion, as further rationalized by DFT calculations and mechanistically confirmed by semi-in situ XPS analysis in the sections that follow.

3.4. Theoretical Insights into Polysulfide Adsorption and Sulfur Redox Kinetics

To establish a mechanistic foundation for the electrochemical performance differences observed between gCN and Fe-SAC@gCN cathodes, and to rationalize the superior performance of the Fe-loaded samples at the atomic scale, DFT calculations were performed on representative gCN and Fe-SAC@gCN model surfaces.

The gCN surface was modeled using the melon-like framework, consistent with the structural characterization presented in previous sections, and with prior evidence establishing the melon-like structure as the thermodynamically preferred phase of gCN.[31,66] For the Fe-SAC@gCN model, an atomically dispersed Fe atom was stabilized within the melon-like gCN framework (Figure 5a). The DFT-optimized Fe-N bond length in the Fe-SAC@gCN model of 1.89 Å is in good agreement with the first-shell Fe-N distances of 1.987–1.998 Å determined experimentally by EXAFS fitting (Table 2), falling within the experimental uncertainty range. This agreement between theory and experiment validates the structural model used for all subsequent calculations and confirms that the DFT surface accurately captures the local coordination environment of the Fe single-atom sites. The same DFT-optimized structural models also served as starting configurations for the EXAFS fitting described previously, ensuring structural consistency between the theoretical and experimental analyses.

The polysulfide adsorption behavior on gCN and Fe-SAC@gCN was evaluated by calculating the adsorption energies of the full series of lithium polysulfide intermediates (Li_2S, Li_2S_2, Li_2S_4, Li_2S_6, and Li_2S_8) using the expression E_{ads} = E (surface) – E (Li_2S_x) – E (surface + Li_2S_x), where positive values indicate favorable adsorption (Figure 5b). Across all polysulfide species, Fe-SAC@gCN exhibits significantly higher adsorption energies than bare gCN. As a representative example, Li_2S_4, the pivotal intermediate at the liquid-to-solid polysulfide transition, adsorbs with an energy of 3.38 eV on Fe-SAC@gCN compared to 1.17 eV on bare gCN, reflecting a substantially stronger chemical interaction at the Fe-N_x site. The enhanced adsorption across all polysulfide species arises

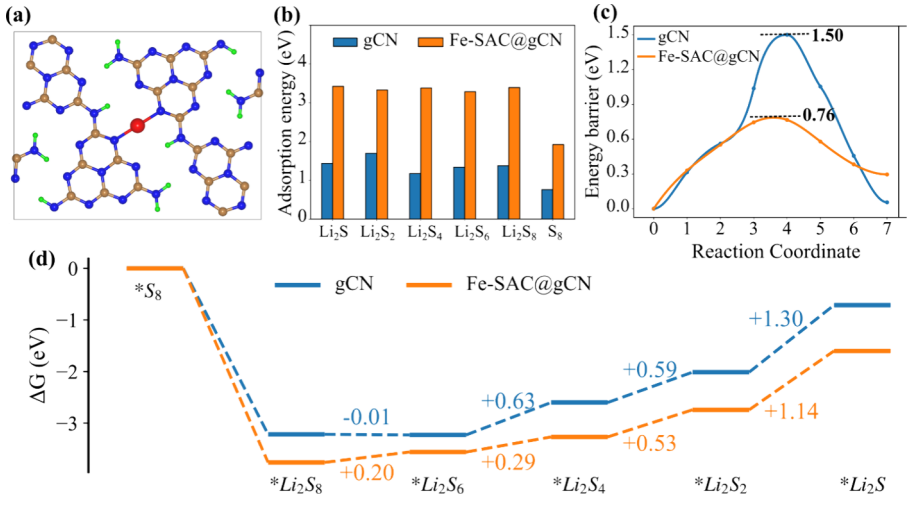


Figure 5. Density functional theory results for gCN and Fe-SAC@gCN. (a) Optimized structure of Fe single atom doped on melon-like gCN. Comparison of adsorption energies (b) of polysulfides adsorbed, decomposition energy (c) of Li_2S, and Gibbs free energy profile (d) of sulfur reduction reaction on surfaces gCN and Fe-SAC@gCN.

Downloaded from pubs.acs.org/aaemcq/article-pdf/doi/10.1021/acsaem.6c02314/68937037/ae-2026-02314j.pdf by CENTRAL MICHIGAN UNIV user on 22 October 2026

https://doi.org/10.1021/acsaem.6c02314
ACS Appl. Energy Mater. XXXX, XXX, XXX–XXX

from strong hybridization between the Fe *3d* orbitals and the S *2p* orbitals of the polysulfide intermediates, highlighting the catalytic role of atomically dispersed Fe sites in promoting polysulfide anchoring.[24,26] The stronger polysulfide adsorption on Fe-SAC@gCN directly accounts for the markedly superior capacity retention observed experimentally for Fe-loaded samples relative to bare gCN supports. This improvement arises because stronger anchoring of soluble polysulfide intermediates at the cathode surface reduces their dissolution and migration into the electrolyte, thereby suppressing the shuttle effect and mitigating irreversible capacity loss. The significantly lower capacity fade observed for the Fe-loaded series compared to bare gCN over 200 cycles is thus mechanistically rooted in this enhancement in polysulfide anchoring.

The thermodynamics of the sulfur reduction reaction (SRR) were analyzed by constructing the Gibbs free energy profile for the stepwise discharge process $S_8 \rightarrow Li_2S_8 \rightarrow Li_2S_6 \rightarrow Li_2S_4 \rightarrow Li_2S_2 \rightarrow Li_2S$ on both gCN and Fe-SAC@gCN surfaces (Figure 5d), and structures of polysulfides adsorbed on both surfaces are shown in Figure S7. The rate-determining step (the electrochemical step with the largest thermodynamic energy barrier) exhibits a barrier of 1.30 eV on bare gCN and is reduced to 1.14 eV on Fe-SAC@gCN, representing a decrease of 0.16 eV upon Fe single-atom incorporation. This lowering of the rate-determining step barrier confirms that the Fe-N_x sites thermodynamically facilitate the sulfur reduction pathway, making the conversion of polysulfide intermediates to Li_2S more energetically favorable.[54,55] Beyond the discharge process, the charging efficiency of Li–S batteries is governed by the ability to decompose the final discharge product Li_2S.[67]

To evaluate this, CI-NEB calculations were performed to determine the Li_2S decomposition energy barrier on both surfaces (Figure 5c), and their corresponding paths are plotted in Figure S8. The decomposition barrier is dramatically reduced from 1.50 eV on bare gCN to 0.76 eV on Fe-SAC@gCN, a decrease of 0.74 eV, representing a near-halving of the barrier upon Fe single-atom incorporation. This reduction indicates that the Fe-N_x sites substantially lower the energetic cost of the rate-limiting charging step, facilitating more efficient oxidation of Li_2S during charge and promoting greater reversibility of the sulfur redox cycle.[23,26] Further, lowering the decomposition energy barrier ensures more complete utilization of the active sulfur during each charge cycle, reducing the accumulation of irreversible Li_2S deposits, consistent with the higher capacity and retention observed for the Fe-loaded samples vs bare gCN after 200 cycles. Taken together, the DFT calculations reveal a threefold catalytic benefit of Fe single-atom incorporation onto the melon-like gCN framework: enhanced chemical adsorption of polysulfide intermediates that suppress shuttle-driven capacity loss, a lowered rate-determining step for the sulfur reduction reaction that accelerates the discharge process, and a reduced decomposition energy barrier of Li_2S that promotes efficient and reversible charging. While the present DFT model represents the experimentally determined coordination environment of the Fe-loaded samples, an explicit computational comparison across different Fe-N coordination numbers, corresponding to the Fe-P and Fe-R series, respectively, would further quantify the coordination–activity relationship and is reserved for future work. The mechanistic picture is further completed by the semi-in situ XPS analysis presented in the following section, which directly tracks the evolution of sulfur species during electrochemical cycling and provides experimental confirmation of the DFT-predicted polysulfide conversion behavior.

3.5. Semi-In Situ XPS Analysis of Sulfur Speciation during Electrochemical Cycling

To directly probe the evolution of sulfur species at different states of charge and to provide experimental confirmation of the DFT-predicted polysulfide conversion behavior, semi-in situ XPS was performed on cathodes at 100% state of charge (SOC, before cycling) and 0% SOC (after 200 cycles). The S *2p* core-level spectra were acquired and deconvoluted into contributions from terminal sulfide species (S^{2-}), terminal polysulfide species (S_T^{1-}), bridging sulfur (S_B^0), and oxidized sulfur species (S-O), reflecting the distribution of sulfur-containing phases present at each state of charge.[32,68,69] The quantitative distribution of sulfur species derived from deconvolution of the S *2p* spectra is summarized in Table 3, with the full XPS survey and core-level spectra of all cathode samples at both SOC states shown in Figures S9–S12.

Table 3. Quantitative Distribution of Sulfur Species Derived from S *2p* XPS Analysis of Bare and Fe-Loaded gCN Cathodes at Different States of Charge (SOC)[a]

sample		terminal S (S^{2-})	bridging S	oxidized S/S^0
u_pCN	100% SOC (before cycling)	-	62.81 %	37.18 %
	0% SOC (200 cycles)	35.0 %	–	64.9 %
Fe-P1	100% SOC (before cycling)	31.0 %	22.34 %	30.0 % (S_8), 16.5 % (S-O)
	0% SOC (200 cycles)	17.8 %	23.8 %	58.3 %
Fe-P2	100% SOC (before cycling)	52.03 %	17.7 %	19.0 % (S_8), 11.24 % (S-O)
	0% SOC (200 cycles)	42.3 %	15.5 %	42.3 %
u_rCN	100% SOC (before cycling)	43.4 %	–	56.5 %
	0% SOC (200 cycles)	31.0 %	–	68.9 %
Fe-R1	100% SOC (before cycling)	59.7%	9.02%	22.79 % (S_8), 8.47 % (S-O)
	0% SOC (200 cycles)	(Li_2S: 45.37 %, other terminally bonded 54.62 %)	–	–
Fe-R2	100% SOC (before cycling)	23.15 %	20.79 %	38.5 % (S_8), 17.4% (S-O)
	0% SOC (200 cycles)	49.4%	–	50.4 %

[a]The relative contributions of terminal sulfide species (S^{2-}), bridging sulfur (S_B^0), and oxidized sulfur species (S^0/S-O) are reported for samples at 100% SOC (before cycling) and 0% SOC after prolonged cycling (200 cycles). Fe-loaded samples exhibit a higher fraction of reduced sulfur species (S^{2-}/terminal sulfur) and a suppressed accumulation of oxidized sulfur species compared to pristine supports, indicating enhanced polysulfide conversion and improved redox reversibility. Notably, the Fe-R1 sample shows significant retention of Li_2S and terminally bonded sulfur species after cycling, further highlighting the role of Fe-N_x active sites in promoting efficient sulfur redox kinetics and mitigating polysulfide shuttling.

https://doi.org/10.1021/acsaem.6c02314
ACS Appl. Energy Mater. XXXX, XXX, XXX–XXX

Downloaded from pubs.acs.org/aaemcq/article-pdf/doi/10.1021/acsaem.6c02314/68937037/ae-2026-02314j.pdf by CENTRAL MICHIGAN UNIV user on 22 October 2026

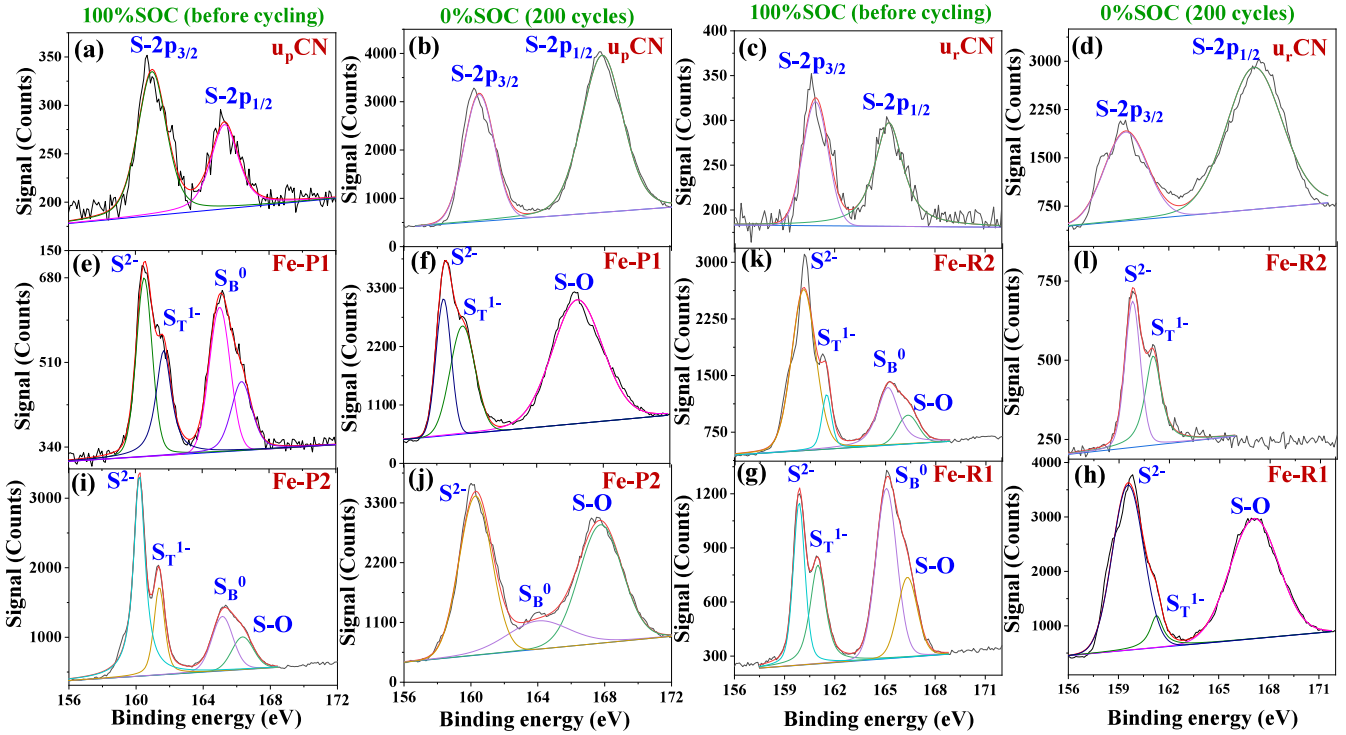


Figure 6. Core-level S *2p* XPS spectra of bare and Fe-loaded gCN cathodes at different states of charge (SOC). Panels (a, e, and i) correspond to u_pCN, Fe-P1, and Fe-P2 at 100% SOC (before cycling), while (b, f, and j) represent the corresponding samples at 0% SOC after prolonged cycling (200 cycles). Similarly, (c, g, and k) correspond to u_rCN, Fe-R1, and Fe-R2 at 100% SOC, and (d, h, and l) show the corresponding samples at 0% SOC after 200 cycles. The deconvoluted spectra reveal contributions from sulfide (S^{2-}), terminal sulfur (S_T^{-1}), bridging sulfur (S_B^0), and oxidized sulfur species (S-O), reflecting the evolution of polysulfide intermediates during electrochemical cycling. Compared to bare gCN supports, Fe-loaded samples exhibit a pronounced shift toward reduced sulfur species (S^{2-}/S_T^{-1}) and a marked suppression of oxidized sulfur species after cycling, indicating accelerated polysulfide conversion kinetics and mitigated shuttle effects. These results strongly support the catalytic role of Fe-N_x active sites in promoting sulfur redox reactions and enhancing electrochemical reversibility.

At 100% SOC (before cycling), the S 2*p* spectra of all samples are dominated by bridging sulfur (S_B^0) and oxidized sulfur species (S–O), consistent with the presence of elemental sulfur (S_8) and long-chain polysulfides as the predominant phases in the fully charged cathode (Table 3 and Figure 6a,c,e,g,i, and k). Among the bare supports, u_pCN shows no terminal S^{2-} contribution at 100% SOC, exhibiting 62.81% bridging S and 37.18% oxidized S. Notably, u_rCN already displays 43.4% terminal S and 56.5% oxidized S at 100% SOC, an observation that reflects the inherently more reductive character of the thermally reduced support even in the absence of Fe, and which is consistent with the modified nitrogen speciation of u_rCN. Among the Fe-loaded samples, measurable terminal sulfide contributions are observed at 100% SOC across all samples: Fe-P1 shows 31.0% S^{2-}, Fe-P2 shows 52.03%, Fe-R1 shows 59.7%, and Fe-R2 shows 23.15% alongside 20.79% bridging S. These findings suggest that the Fe-N_x sites promote partial retention of reduced sulfur species even in the charged state, consistent with the stronger polysulfide adsorption established by DFT. The 100% SOC values do not vary monotonically with Fe loading or coordination number, so these spectra are treated as a baseline against which the discharged state is compared rather than as a measure of catalytic activity. Their retention of terminal sulfide nonetheless raises the question of whether anchoring at Fe-N_x sites could impede Li_2S oxidation and strand sulfur; adsorption energies cannot settle this, as they describe binding rather than release, and desorption free energies were not computed here. Two observations argue against over-binding: the Li_2S decomposition barrier is approximately halved on Fe-SAC@gCN relative to bare gCN (Section 3.4), and over 200 cycles, the Coulombic efficiency of all Fe-loaded cathodes remains above 95% without progressive decline (Figure 3g and h), while the Fe-R series shows the lowest capacity-fade rates of any sample examined.

The most mechanistically informative differences emerge at 0% SOC after 200 cycles (Figure 6b, d, f, h, j, and l), where the S 2*p* spectra directly reflect the degree of polysulfide conversion achieved during discharge. For bare gCN supports, the 0% SOC spectra are dominated by oxidized sulfur species, u_pCN retains 64.9% S-O with only 35.0% terminal S^{2-}, while u_rCN shows 68.9% S-O with 31.0% terminal S^{2-}, indicating substantial accumulation of incompletely converted sulfur species after full nominal discharge. This large residual oxidized sulfur fraction is consistent with sluggish polysulfide conversion kinetics on the bare supports, corroborating the poor capacity retention and high polarization observed electrochemically, and the elevated thermodynamic barriers predicted by DFT. In contrast, all Fe-loaded samples exhibit a pronounced shift toward reduced sulfur species at 0% SOC, with markedly suppressed accumulation of oxidized sulfur relative to their bare gCN counterparts. Within the pristine support series, Fe-P1 retains 17.8% terminal S^{2-} and 23.8% bridging S at 0% SOC with 58.3% oxidized S, while Fe-P2 shows substantially improved conversion with 42.3% terminal S^{2-}, 15.5% bridging S, and

Downloaded from pubs.acs.org/aaemcq/article-pdf/doi/10.1021/acsaem.6c02314/68937037/ae-2026-02314j.pdf by CENTRAL MICHIGAN UNIV user on 22 October 2026

https://doi.org/10.1021/acsaem.6c02314
ACS Appl. Energy Mater. XXXX, XXX, XXX–XXX

42.3% oxidized S. The most compelling results are observed in the reduced support series. Fe-R2 achieves 49.4% terminal S^{2-} at 0% SOC with correspondingly suppressed oxidized sulfur (50.4%), while Fe-R1 delivers the most efficient polysulfide conversion of all samples: the 0% SOC spectrum is entirely accounted for by Li_2S (45.37%) and other terminally bonded sulfur species (54.62%), with essentially no detectable oxidized sulfur fraction. This highly efficient conversion reaction to terminal sulfide species in Fe-R1 represents direct and unambiguous experimental confirmation that the coordinatively unsaturated Fe-N_x sites of the thermally reduced series catalyze the full reduction of polysulfide intermediates to Li_2S during discharge, precisely as predicted by the DFT Gibbs free energy profiles and the lowered rate-determining step barrier. At the series level, the Fe-R cathodes show the highest terminal sulfide fractions at 0% SOC (Table 3), consistent with their superior capacity retention and rate capability. The ordering is not strictly monotonic across individual samples; however, Fe-P1 retains the smallest terminal sulfide fraction of any cathode examined despite outperforming Fe-P2 electrochemically. Fe-P1 combines the lowest Fe content of the four catalysts (Table S2) with the near-saturated first-shell coordination characteristic of the pristine support (1.89, Table 2), giving the lowest density of catalytically active sites, and its spectrum is correspondingly dominated by oxidized sulfur (58.3%). Because XPS probes only the outermost few nanometers of a single harvested electrode, surface sulfate- and sulfite-type overlayers can obscure the underlying conversion state, so the comparison between the two series is more robust than that between individual samples within a series. The suppression of oxidized sulfur accumulation in the Fe-R series is further consistent with the near-halving of the Li_2S decomposition barrier on Fe-SAC@gCN established by CI-NEB calculations, which ensures that Li_2S formed during discharge is efficiently decomposed during charging, preventing the buildup of electrochemically inactive sulfur deposits that would otherwise contribute to progressive capacity fade.[23,54,69]

Taken together, the semi-in situ XPS analysis provides direct experimental evidence for the catalytic role of Fe-N_x sites in promoting complete and reversible polysulfide conversion. The quantitative S 2*p* speciation data at 0% SOC establish a consistent relationship at the series level between Fe-N_x catalytic activity, modulated by the coordination number and support thermal reduction, and the degree of polysulfide conversion achieved during discharge. Collectively, these observations establish a coherent and mutually corroborating multiscale picture of the Fe-N_x/gCN system: the structural characterization identifies the active site, the electrochemical analysis quantifies its performance implications, the DFT calculations provide the mechanistic rationale at the atomic level, and the semi-in situ XPS presented here closes the loop by directly visualizing the catalytic conversion of polysulfide intermediates under real electrochemical cycling conditions and the persistence of reduced sulfur species after recharging with the coordinative unsaturation of the Fe-N_x sites, establishing a self-consistent mechanistic picture.

4. CONCLUSIONS

In summary, this work demonstrates that the thermal reduction of the urea-derived gCN support is an effective and synthetically straightforward strategy for tuning the local coordination environment of Fe single-atom catalysts, with direct and quantifiable consequences for polysulfide conversion efficiency and Li–S battery performance. Fe-N_x single-atom catalysts were synthesized on both pristine (u_pCN) and thermally reduced (u_rCN) melon-like gCN supports and characterized by a comprehensive multitechnique approach. EXAFS analysis reveals that the thermal reduction of the support systematically lowers the average Fe-N coordination number from ∼1.9 in the Fe-P series to ∼1.1–1.4 in the Fe-R series, producing more coordinatively unsaturated Fe-N_x environments without disrupting the broader melon-like framework. This structural distinction, mechanistically rooted in the modification of the nitrogen speciation of the support established by XPS, translates directly into superior electrochemical performance. Fe-R1 delivers an initial discharge capacity of 693.5 mAh g^{-1} with ∼71% retention over 200 cycles at C/10, outperforming the pristine support series across all metrics. DFT calculations on representative melon-like gCN and Fe-SAC@gCN surfaces reveal a threefold catalytic advantage of Fe single-atom incorporation; stronger polysulfide adsorption energies that suppress shuttle-driven capacity loss, a reduced rate-determining thermodynamic barrier for the sulfur reduction reaction (from 1.30 to 1.14 eV), and a lowered Li_2S decomposition barrier (from 1.50 to 0.76 eV) that promotes efficient and reversible charging. Each of these theoretical predictions is directly confirmed by the semi-in situ S 2*p* XPS analysis, which reveals near-complete conversion of polysulfide intermediates to terminal sulfide species (Li_2S + terminally bonded S: 100%) at 0% SOC for Fe-R1 after 200 cycles, compared to residual oxidized sulfur fractions exceeding 65–69% for bare gCN supports under the same conditions. To the best of our knowledge, this is the first study to employ semi-in situ XPS to directly visualize polysulfide speciation in Fe-N_x/gCN cathodes and to systematically correlate Fe-N coordination number, tuned via support thermal reduction, with polysulfide conversion efficiency at the molecular level. The results establish coordinative unsaturation of Fe-N_x/gCN sites as a key structural descriptor governing Li–S battery performance, and demonstrate that the thermal reduction of the melon-like gCN support is a practical and scalable lever for engineering this property. Beyond Li–S batteries, the coordination engineering approach demonstrated here, leveraging support modification to tune single-atom coordination geometry without disrupting the host framework, is broadly applicable to single-atom catalysts for other sulfur-based and polyanion electrochemical systems where metal–ligand coordination directly governs intermediate adsorption and catalytic conversion. This work provides both mechanistic insights and a rational design principle for the development of next-generation single-atom electrocatalysts for high-performance energy storage.

■ ASSOCIATED CONTENT

Data Availability Statement

All data supporting the findings of this study are available within the article and its supplementary information (SI). Additional raw data or materials can be provided by the corresponding author upon reasonable request.

Supporting Information

The Supporting Information is available free of charge at https://pubs.acs.org/doi/10.1021/acsaem.6c02314.

Comparative XRD patterns, Raman spectra, and SEM images of pristine and reduced gCN and their Fe-

Downloaded from pubs.acs.org/aaemcq/article-pdf/doi/10.1021/acsaem.6c02314/6893037/ae-2026-02314j.pdf by CENTRAL MICHIGAN UNIV user on 22 October 2026

https://doi.org/10.1021/acsaem.6c02314
ACS Appl. Energy Mater. XXXX, XXX, XXX–XXX

loaded samples; XPS survey and core-level spectra of powder samples with and without Fe on pristine and reduced supports; TEM images of Fe-loaded gCN samples, Fourier-transformed EXAFS spectra in R-space (phase-corrected) for Fe-loaded gCN samples and reference compounds (Fe_2O_3, FeO and Fe foil); comparison of capacity retention of Li–S batteries based on various cathode materials in literature vs current study; adsorption of polysulfides (Li_2S, Li_2S_2, Li_2S_4, Li_2S_6, and Li_2S_8) on gCN and Fe-SAC@gCN; Li_2S decomposition energy barrier path on surface gCN and Fe-SAC@gCN; XPS spectra of bare and Fe-loaded u_pCN cathodes at 100% state of charge; XPS spectra of bare and Fe-loaded u_pCN cathodes at 0% state of charge; XPS spectra of bare and Fe-loaded u_rCN cathodes at 100% state of charge; XPS spectra of bare and Fe-loaded u_rCN cathodes at 0% state of charge; synthesis parameters for Fe single-atom catalyst samples; elemental composition (weight percent) of pristine and reduced gCN and their Fe-loaded samples; relative contributions of the deconvoluted N *1s* components for the gCN supports and their Fe-loaded counterparts; and tabulated capacity retention for representative Li–S battery cathode materials reported in the literature alongside the SAC-Fe on the reduced gCN system from this work (DOCX)

■ AUTHOR INFORMATION

Corresponding Authors

Jyoti Pandey – *Department of Physics, Central Michigan University, Mt. Pleasant, Michigan 48859, United States;* orcid.org/0000-0003-3315-5335; Email: pande2j@cmich.edu, jyotipandey51092@gmail.com

Bradley D. Fahlman – *Department of Chemistry and Biochemistry, Central Michigan University, Mt. Pleasant, Michigan 48859, United States;* Email: fahlm1b@cmich.edu

Valeri Petkov – *Department of Physics, Central Michigan University, Mt. Pleasant, Michigan 48859, United States;* orcid.org/0000-0002-6392-7589; Email: petko1vg@cmich.edu

Authors

Aliakbar Yazdani – *Department of Chemistry and Biochemistry, Central Michigan University, Mt. Pleasant, Michigan 48859, United States*

Mukesh Singh – *Department of Physics, Central Michigan University, Mt. Pleasant, Michigan 48859, United States;* orcid.org/0000-0002-1500-6857

Isaac Newton Boakye – *Department of Chemistry and Biochemistry, Central Michigan University, Mt. Pleasant, Michigan 48859, United States;* orcid.org/0009-0002-8894-4411

Kyle Linford Kilbarger – *Department of Chemistry and Biochemistry, Central Michigan University, Mt. Pleasant, Michigan 48859, United States*

Carlos Chavez – *Department of Physics, Central Michigan University, Mt. Pleasant, Michigan 48859, United States*

Zachary Jasper – *Department of Physics, Central Michigan University, Mt. Pleasant, Michigan 48859, United States*

Benjamin R. Seltin – *Department of Materials Science and Engineering, University of Michigan, Ann Arbor, Michigan 48109, United States*

Adeel Zafar – *Department of Physics, Central Michigan University, Mt. Pleasant, Michigan 48859, United States*

Veronica Barone – *Department of Physics, Central Michigan University, Mt. Pleasant, Michigan 48859, United States;* orcid.org/0000-0002-5881-3640

Mark Wolfman – *X-Ray Science Division, Argonne National Laboratory, Lemont, Illinois 60439, United States*

Chi-Hao Chang – *The Dow Chemical Company, Dow Performance Silicones, 5300 11 Mile Road, Auburn, Michigan 48611, United States*

Yi Ding – *U.S. Army Combat Capabilities Development Command (DEVCOM) - Ground Vehicle Systems Center (GVSC), Warren, Michigan 48397, United States*

Complete contact information is available at: https://pubs.acs.org/doi/10.1021/acsaem.6c02314

Author Contributions

J.P. conceived the study, designed, and performed the experiments, conducted the formal analysis, and prepared the original manuscript draft. A.Y., I.N.B., K.L.K., and B.R.S. carried out the electrochemical measurements and corroborated the electrochemical results. M.S. and Z.J. performed the DFT calculations and integrated them with the experimental findings. C.C. analyzed the magnetic data and contributed to manuscript review. A.Z. helped with the EXAFS fittings and analysis. V.B., B.D.F., V.P., C.-H.C., and Y.D. supervised the work and contributed to experimental design, data interpretation, and manuscript review. M.W. assisted with data acquisition and contributed to discussions and manuscript review. All authors have reviewed and approved the final version of the manuscript.

Notes

The authors declare no competing financial interest.

■ ACKNOWLEDGMENTS

The authors acknowledge the support of the Automotive Research Center (ARC), Cooperative Agreement W56HZV-24-2-0001 U.S. Army DEVCOM GVSC. DISTRIBUTION STATEMENT A. Approved for public release; distribution is unlimited. OPSEC#10666. The authors acknowledge the microscopy facility at the Faculty of Biology, Central Michigan University, for the morphological studies. Michigan Center for Materials Characterization, University of Michigan, is also acknowledged for the XPS measurements. The authors also acknowledge computational resources and services provided by the Institute for Cyber-Enabled Research at Michigan State University. This research was performed on APS beam time award(s) (DOI: 10.46936/APS-191790/60015506) from the Advanced Photon Source, a U.S. Department of Energy (DOE) Office of Science user facility operated for the DOE Office of Science by the Argonne National Laboratory under Contract No. DE-AC02-06CH11357.

■ ABBREVIATIONS

gCN	graphitic carbon nitride
u_pCN	urea-derived pristine graphitic carbon nitride
u_rCN	urea-derived reduced graphitic carbon nitride
LiPSs	lithium polysulfides

Downloaded from pubs.acs.org/aaemcq/article-pdf/doi/10.1021/acsaem.6c02314/6893037/ae-2026-02314j.pdf by CENTRAL MICHIGAN UNIV user on 22 October 2026

Fe-P1	lower concentration of Iron deposited on pristine graphitic carbon nitride
Fe-P2	higher concentration of Iron deposited on pristine graphitic carbon nitride
Fe-R1	lower concentration of Iron deposited on reduced graphitic carbon nitride
Fe-R2	higher concentration of Iron deposited on reduced graphitic carbon nitride
Fe-N_x	single-atom Iron attached to nitrogen of graphitic carbon nitride
Fe-SACs	single-atom catalysts

REFERENCES

(1) Griffith, K. J.; Wiaderek, K. M.; Cibin, G.; Marbella, L. E.; Grey, C. P. Niobium Tungsten Oxides for High-Rate Lithium-Ion Energy Storage. *Nature* **2018**, *559*, 556–563.

(2) Zhang, M.; Xiang, L.; Galluzzi, M.; Jiang, C.; Zhang, S.; Li, J.; Tang, Y. Uniform Distribution of Alloying/Dealloying Stress for High Structural Stability of an Al Anode in High-Areal-Density Lithium-Ion Batteries. *Adv. Mater.* **2019**, *31*, 1900826.

(3) Bruce, P. G.; Freunberger, S. A.; Hardwick, L. J.; Tarascon, J.-M. Li-O2 and Li-S Batteries with High Energy Storage. *Nat. Mater.* **2012**, *11*, 19–29.

(4) Manthiram, A.; Fu, Y.; Chung, S.-H.; Zu, C.; Su, Y.-S. Rechargeable Lithium-Sulfur Batteries. *Chem. Rev.* **2014**, *114*, 11751–11787.

(5) Peng, H.-J.; Huang, J.-Q.; Cheng, X.-B.; Zhang, Q. Review on High-Loading and High-Energy Lithium-Sulfur Batteries. *Adv. Energy Mater.* **2017**, *7*, 1700260.

(6) Ji, X.; Lee, K. T.; Nazar, L. F. A Highly Ordered Nanostructured Carbon-Sulphur Cathode for Lithium-Sulphur Batteries. *Nat. Mater.* **2009**, *8*, 500–506.

(7) Manthiram, A.; Fu, Y.; Su, Y.-S. Challenges and Prospects of Lithium-Sulfur Batteries. *Acc. Chem. Res.* **2013**, *46*, 1125–1134.

(8) Lu, C.; Fang, R.; Chen, X. Single-Atom Catalytic Materials for Advanced Battery Systems. *Adv. Mater.* **2020**, *32*, 1906548.

(9) Zhou, T.; Liang, J.; Ye, S.; Zhang, Q.; Liu, J. Fundamental, Application and Opportunities of Single Atom Catalysts for Li-S Batteries. *Energy Storage Mater.* **2023**, *55*, 322–355.

(10) Hencz, L.; Chen, H.; Ling, H. Y.; Wang, Y.; Lai, C.; Zhao, H.; Zhang, S. Housing Sulfur in Polymer Composite Frameworks for Li-S Batteries. *Nano-Micro Lett.* **2019**, *11*, 17.

(11) Pang, Q.; Liang, X.; Kwok, C. Y.; Nazar, L. F. Advances in Lithium-Sulfur Batteries Based on Multifunctional Cathodes and Electrolytes. *Nat. Energy* **2016**, *1*, 16132.

(12) Jin, J.; Cai, W.; Cai, J.; Shao, Y.; Song, Y.; Xia, Z.; Zhang, Q.; Sun, J. MOF-Derived Hierarchical CoP Nanoflakes Anchored on Vertically Erected Graphene Scaffolds as Self-Supported and Flexible Hosts for Lithium-Sulfur Batteries. *J. Mater. Chem. A* **2020**, *8*, 3027–3034.

(13) Shi, Z.; Sun, Z.; Cai, J.; Fan, Z.; Jin, J.; Wang, M.; Sun, J. Boosting Dual-Directional Polysulfide Electrocatalysis via Bimetallic Alloying for Printable Li-S Batteries. *Adv. Funct. Mater.* **2021**, *31*, 2006798.

(14) Zhao, M.; Li, B.-Q.; Zhang, X.-Q.; Huang, J.-Q.; Zhang, Q. A Perspective toward Practical Lithium-Sulfur Batteries. *ACS Cent. Sci.* **2020**, *6*, 1095–1104.

(15) Fang, R.; Chen, K.; Yin, L.; Sun, Z.; Li, F.; Cheng, H. The Regulating Role of Carbon Nanotubes and Graphene in Lithium-Ion and Lithium-Sulfur Batteries. *Adv. Mater.* **2019**, *31*, 1800863.

(16) Xu, Z.-L.; Kim, J.-K.; Kang, K. Carbon Nanomaterials for Advanced Lithium Sulfur Batteries. *Nano Today* **2018**, *19*, 84–107.

(17) Geng, H.; Peng, Y.; Qu, L.; Zhang, H.; Wu, M. Structure Design and Composition Engineering of Carbon-Based Nanomaterials for Lithium Energy Storage. *Adv. Energy Mater.* **2020**, *10*, 1903030.

(18) Wu, X.; Liu, N.; Wang, M.; Qiu, Y.; Guan, B.; Tian, D.; Guo, Z.; Fan, L.; Zhang, N. A Class of Catalysts of BiOX (X = Cl, Br, I) for Anchoring Polysulfides and Accelerating Redox Reaction in Lithium Sulfur Batteries. *ACS Nano* **2019**, *13*, 13109–13115.

(19) Liang, Z.; Shen, J.; Xu, X.; Li, F.; Liu, J.; Yuan, B.; Yu, Y.; Zhu, M. Advances in the Development of Single-Atom Catalysts for High-Energy-Density Lithium-Sulfur Batteries. *Adv. Mater.* **2022**, *34*, 2200102.

(20) Speck, F. D.; Kim, J. H.; Bae, G.; Joo, S. H.; Mayrhofer, K. J. J.; Choi, C. H.; Cherevko, S. Single-Atom Catalysts: A Perspective toward Application in Electrochemical Energy Conversion. *JACS Au* **2021**, *1*, 1086–1100.

(21) Song, Y.; Zou, L.; Wei, C.; Zhou, Y.; Hu, Y. Single-Atom Electrocatalysts for Lithium-Sulfur Chemistry: Design Principle, Mechanism, and Outlook. *Carbon Energy* **2023**, *5*, e286.

(22) Li, L.; Xiao, J.; Zhao, G.; Xu, J.; Xia, S.; Li, X.; Pang, Y.; Yang, J.; Sun, H.; Yuan, T.; Zheng, S. Dual-Atom Catalysts for Lithium-Sulfur Battery Cathodes: Synthesis, Characterization, and Catalytic Mechanisms. *Mater. Rep. Energy* **2026**, *6*, 100451.

(23) He, S.; Yang, J.; Liu, S.; Wang, X.; Che, X.; Wang, M.; Qiu, J. Asymmetric N-Coordinated Iron Single-Atom Catalysts Supported on Graphitic Carbon for Polysulfide Conversion in Lithium-Sulfur Batteries. *Chem. Eng. J.* **2023**, *454*, 140202.

(24) Qiu, Y.; Fan, L.; Wang, M.; Yin, X.; Wu, X.; Sun, X.; Tian, D.; Guan, B.; Tang, D.; Zhang, N. Precise Synthesis of Fe-N2 Sites with High Activity and Stability for Long-Life Lithium-Sulfur Batteries. *ACS Nano* **2020**, *14*, 16105–16113.

(25) Lu, C.; Chen, Y.; Yang, Y.; Chen, X. Single-Atom Catalytic Materials for Lean-Electrolyte Ultrastable Lithium-Sulfur Batteries. *Nano Lett.* **2020**, *20*, 5522–5530.

(26) Ding, Y.; Cheng, Q.; Wu, J.; Yan, T.; Shi, Z.; Wang, M.; Yang, D.; Wang, P.; Zhang, L.; Sun, J. Enhanced Dual-Directional Sulfur Redox via a Biotemplated Single-Atomic Fe-N2 Mediator Promises Durable Li-S Batteries. *Adv. Mater.* **2022**, *34*, 2202256.

(27) Sun, H.; Li, L.; Zhu, Z.; Li, X.; Zhu, Z.; Yuan, T.; Yang, J.; Pang, Y.; Zheng, S. Vacancy-Defective Nano-Carbon Matrix Enables Highly Efficient Fe Single Atom Catalyst for Aqueous and Flexible Zn-Air Batteries. *Chem. Eng. J.* **2024**, *496*, 153669.

(28) Zhou, Y.; Tao, X.; Chen, G.; Lu, R.; Wang, D.; Chen, M.-X.; Jin, E.; Yang, J.; Liang, H.-W.; Zhao, Y.; Feng, X.; Narita, A.; Müllen, K. Multilayer Stabilization for Fabricating High-Loading Single-Atom Catalysts. *Nat. Commun.* **2020**, *11*, 5892.

(29) Rocha, G. F. S. R.; Da Silva, M. A. R.; Rogolino, A.; Diab, G. A. A.; Noleto, L. F. G.; Antonietti, M.; Teixeira, I. F. Carbon Nitride Based Materials: More Than Just a Support for Single-Atom Catalysis. *Chem. Soc. Rev.* **2023**, *52*, 4878–4932.

(30) P, S.; John, J.; Rajan, T. P. D.; Anilkumar, G. M.; Yamaguchi, T.; Pillai, S. C.; Hareesh, U. S. Graphitic Carbon Nitride ($g\text{-}C_3N_4$) Based Heterogeneous Single Atom Catalysts: Synthesis, Characterisation and Catalytic Applications. *J. Mater. Chem. A* **2023**, *11*, 8599–8646.

(31) Pandey, J.; Yazdani, A.; Jakhar, M.; Petkov, V.; Barone, V.; Chang, C.-H.; Caruntu, G.; Ding, Y.; Fahlman, B. D. From Structure to Functional Implications: Investigation of the Melon-like Framework of Graphitic Carbon Nitride for Li-S Batteries. *ACS Omega* **2025**, *10*, 47375–47385.

(32) Yu, J.; Pinto-Huguet, I.; Zhang, C. Y.; Zhou, Y.; Xu, Y.; Vizintin, A.; Velasco-Vélez, J.-J.; Qi, X.; Pan, X.; Oney, G.; Olgo, A.; Märker, K.; Da Silva, L. M.; Luo, Y.; Lu, Y.; Huang, C.; Härk, E.; Fleming, J.; Chenevier, P.; Cabot, A.; Bai, Y.; Botifoll, M.; Black, A. P.; An, Q.; Amietszajew, T.; Arbiol, J. Mechanistic Insights and Technical Challenges in Sulfur-Based Batteries: A Comprehensive in Situ/Operando Monitoring Toolbox. *ACS Energy Lett.* **2024**, *9*, 6178–6214.

(33) Ravel, B.; Newville, M. ATHENA, ARTEMIS, HEPHAESTUS: Data Analysis for X-ray Absorption Spectroscopy Using IFEFFIT. *J. Synchrotron Radiat.* **2005**, *12*, 537–541.

(34) Rehr, J. J.; Albers, R. C. Theoretical Approaches to X-ray Absorption Fine Structure. *Rev. Mod. Phys.* **2000**, *72*, 621–654.

(35) Rehr, J. J.; Mustre De Leon, J.; Zabinsky, S. I.; Albers, R. C. Theoretical X-ray Absorption Fine Structure Standards. *J. Am. Chem. Soc.* **1991**, *113*, 5135–5140.

Downloaded from pubs.acs.org/aaemcq/article-pdf/doi/10.1021/acsaem.6c02314/68937037/ae-2026-02314j.pdf by CENTRAL MICHIGAN UNIV user on 22 October 2026

https://doi.org/10.1021/acsaem.6c02314
ACS Appl. Energy Mater. XXXX, XXX, XXX–XXX

(36) Kresse, G.; Furthmüller, J. Efficient Iterative Schemes for Ab Initio Total-Energy Calculations Using a Plane-Wave Basis Set. *Phys. Rev. B* **1996**, *54*, 11169–11186.
(37) Kresse, G.; Furthmüller, J. Efficiency of Ab-Initio Total Energy Calculations for Metals and Semiconductors Using a Plane-Wave Basis Set. *Comput. Mater. Sci.* **1996**, *6*, 15–50.
(38) Kresse, G.; Joubert, D. From Ultrasoft Pseudopotentials to the Projector Augmented-Wave Method. *Phys. Rev. B* **1999**, *59*, 1758–1775.
(39) Grimme, S.; Ehrlich, S.; Goerigk, L. Effect of the Damping Function in Dispersion Corrected Density Functional Theory. *J. Comput. Chem.* **2011**, *32*, 1456–1465.
(40) Geng, W.-T.; Liu, Y.-C.; Xu, N.; Tang, G.; Kawazoe, Y.; Wang, V. Empowering Materials Science with VASPKIT: A Toolkit for Enhanced Simulation and Analysis. *Nat. Protoc.* **2025**, *20*, 3143–3169.
(41) Henkelman, G.; Uberuaga, B. P.; Jónsson, H. A Climbing Image Nudged Elastic Band Method for Finding Saddle Points and Minimum Energy Paths. *J. Chem. Phys.* **2000**, *113*, 9901–9904.
(42) Henkelman, G.; Jónsson, H. Improved Tangent Estimate in the Nudged Elastic Band Method for Finding Minimum Energy Paths and Saddle Points. *J. Chem. Phys.* **2000**, *113*, 9978–9985.
(43) Li, J.; Karjule, N.; Qin, J.; Wang, Y.; Barrio, J.; Shalom, M. Low-Temperature Synthesis of Solution Processable Carbon Nitride Polymers. *Molecules* **2021**, *26*, 1646.
(44) An, S.; Zhang, G.; Wang, T.; Zhang, W.; Li, K.; Song, C.; Miller, J. T.; Miao, S.; Wang, J.; Guo, X. High-Density Ultra-Small Clusters and Single-Atom Fe Sites Embedded in Graphitic Carbon Nitride (g-C3N4) for Highly Efficient Catalytic Advanced Oxidation Processes. *ACS Nano* **2018**, *12*, 9441–9450.
(45) Bagus, P. S.; Nelin, C. J.; Brundle, C. R.; Lahiri, N.; Ilton, E. S.; Rosso, K. M. Analysis of the Fe 2p XPS for Hematite α-Fe2O3: Consequences of Covalent Bonding and Orbital Splittings on Multiplet Splittings. *J. Chem. Phys.* **2020**, *152*, 014704.
(46) Yamashita, T.; Hayes, P. Analysis of XPS Spectra of Fe2+ and Fe3+ Ions in Oxide Materials. *Appl. Surf. Sci.* **2008**, *254*, 2441–2449.
(47) Mo, F.; Song, C.; Zhou, Q.; Xue, W.; Ouyang, S.; Wang, Q.; Hou, Z.; Wang, S.; Wang, J. The Optimized Fenton-like Activity of Fe Single-Atom Sites by Fe Atomic Clusters-Mediated Electronic Configuration Modulation. *Proc. Natl. Acad. Sci. U. S. A.* **2023**, *120*, e2300281120.
(48) Mugiraneza, S.; Hallas, A. M. Tutorial: A Beginner's Guide to Interpreting Magnetic Susceptibility Data with the Curie-Weiss Law. *Commun. Phys.* **2022**, *5*, 95.
(49) Chen, Z.; Walsh, A. G.; Zhang, P. Structural Analysis of Single-Atom Catalysts by X-ray Absorption Spectroscopy. *Acc. Chem. Res.* **2024**, *57*, 521–532.
(50) Zhang, L.; Yang, X.; Lin, J.; Li, X.; Liu, X.; Qiao, B.; Wang, A.; Zhang, T. On the Coordination Environment of Single-Atom Catalysts: Pioneer Account. *Acc. Chem. Res.* **2025**, *58*, 1878–1892.
(51) Zitolo, A.; Goellner, V.; Armel, V.; Sougrati, M.-T.; Mineva, T.; Stievano, L.; Fonda, E.; Jaouen, F. Identification of Catalytic Sites for Oxygen Reduction in Iron- and Nitrogen-Doped Graphene Materials. *Nat. Mater.* **2015**, *14*, 937–942.
(52) Pan, Y.; Chen, Y.; Wu, K.; Chen, Z.; Liu, S.; Cao, X.; Cheong, W.-C.; Meng, T.; Luo, J.; Zheng, L.; Liu, C.; Wang, D.; Peng, Q.; Li, J.; Chen, C. Regulating the Coordination Structure of Single-Atom Fe-N_xC_y Catalytic Sites for Benzene Oxidation. *Nat. Commun.* **2019**, *10*, 4290.
(53) Sarma, B. B.; Maurer, F.; Doronkin, D. E.; Grunwaldt, J.-D. Design of Single-Atom Catalysts and Tracking Their Fate Using Operando and Advanced X-ray Spectroscopic Tools. *Chem. Rev.* **2023**, *123*, 379–444.
(54) Song, W.; Wen, Z.; Wang, X.; Qian, K.; Zhang, T.; Wang, H.; Ding, J.; Hu, W. Unsaturation Degree of Fe Single Atom Site Manipulates Polysulfide Behavior in Sodium-Sulfur Batteries. *Nat. Commun.* **2025**, *16*, 2795.
(55) Liu, G.; Wang, W.; Zeng, P.; Yuan, C.; Wang, L.; Li, H.; Zhang, H.; Sun, X.; Dai, K.; Mao, J.; Li, X.; Zhang, L. Strengthened d-p Orbital Hybridization through Asymmetric Coordination Engineering of Single-Atom Catalysts for Durable Lithium-Sulfur Batteries. *Nano Lett.* **2022**, *22*, 6366–6374.
(56) Yeon, J. S.; Yun, S.; Park, J. M.; Park, H. S. Surface-Modified Sulfur Nanorods Immobilized on Radially Assembled Open-Porous Graphene Microspheres for Lithium-Sulfur Batteries. *ACS Nano* **2019**, *13*, 5163–5171.
(57) Tian, W.; Xi, B.; Feng, Z.; Li, H.; Feng, J.; Xiong, S. Sulfiphilic Few-Layered $MoSe_2$ Nanoflakes Decorated rGO as a Highly Efficient Sulfur Host for Lithium-Sulfur Batteries. *Adv. Energy Mater.* **2019**, *9*, 1901896.
(58) Hua, W.; Yang, Z.; Nie, H.; Li, Z.; Yang, J.; Guo, Z.; Ruan, C.; Chen, X.; Huang, S. Polysulfide-Scission Reagents for the Suppression of the Shuttle Effect in Lithium-Sulfur Batteries. *ACS Nano* **2017**, *11*, 2209–2218.
(59) Peng, H.-J.; Zhang, G.; Chen, X.; Zhang, Z.-W.; Xu, W.-T.; Huang, J.-Q.; Zhang, Q. Enhanced Electrochemical Kinetics on Conductive Polar Mediators for Lithium–Sulfur Batteries. *Angew. Chem., Int. Ed.* **2016**, *55*, 12990–12995.
(60) Du, Z.; Chen, X.; Hu, W.; Chuang, C.; Xie, S.; Hu, A.; Yan, W.; Kong, X.; Wu, X.; Ji, H.; Wan, L.-J. Cobalt in Nitrogen-Doped Graphene as Single-Atom Catalyst for High-Sulfur Content Lithium-Sulfur Batteries. *J. Am. Chem. Soc.* **2019**, *141*, 3977–3985.
(61) Wang, T.; Zhu, J.; Wei, Z.; Yang, H.; Ma, Z.; Ma, R.; Zhou, J.; Yang, Y.; Peng, L.; Fei, H.; Lu, B.; Duan, X. Bacteria-Derived Biological Carbon Building Robust Li-S Batteries. *Nano Lett.* **2019**, *19*, 4384–4390.
(62) Wang, Y.; Adekoya, D.; Sun, J.; Tang, T.; Qiu, H.; Xu, L.; Zhang, S.; Hou, Y. Manipulation of Edge-Site Fe-N2 Moiety on Holey Fe, N Codoped Graphene to Promote the Cycle Stability and Rate Capacity of Li-S Batteries. *Adv. Funct. Mater.* **2019**, *29*, 1807485.
(63) Lim, W.-G.; Mun, Y.; Cho, A.; Jo, C.; Lee, S.; Han, J. W.; Lee, J. Synergistic Effect of Molecular-Type Electrocatalysts with Ultrahigh Pore Volume Carbon Microspheres for Lithium-Sulfur Batteries. *ACS Nano* **2018**, *12*, 6013–6022.
(64) Wang, J.; Jia, L.; Zhong, J.; Xiao, Q.; Wang, C.; Zang, K.; Liu, H.; Zheng, H.; Luo, J.; Yang, J.; Fan, H.; Duan, W.; Wu, Y.; Lin, H.; Zhang, Y. Single-Atom Catalyst Boosts Electrochemical Conversion Reactions in Batteries. *Energy Storage Mater.* **2019**, *18*, 246–252.
(65) Choi, M.; Jo, J.; Eom, K. Polarity Modification of Graphitic Carbon Nitride for the Mitigation of the Shuttle Effect in Lithium-Sulfur Batteries. *ACS Appl. Energy Mater.* **2025**, *8*, 6707–6712.
(66) Fina, F.; Callear, S. K.; Carins, G. M.; Irvine, J. T. S. Structural Investigation of Graphitic Carbon Nitride via XRD and Neutron Diffraction. *Chem. Mater.* **2015**, *27*, 2612–2618.
(67) Zhou, G.; Tian, H.; Jin, Y.; Tao, X.; Liu, B.; Zhang, R.; Seh, Z. W.; Zhuo, D.; Liu, Y.; Sun, J.; Zhao, J.; Zu, C.; Wu, D. S.; Zhang, Q.; Cui, Y. Catalytic Oxidation of Li_2S on the Surface of Metal Sulfides for Li-S Batteries. *Proc. Natl. Acad. Sci. U. S. A.* **2017**, *114*, 840–845.
(68) Nandasiri, M. I.; Camacho-Forero, L. E.; Schwarz, A. M.; Shutthanandan, V.; Thevuthasan, S.; Balbuena, P. B.; Mueller, K. T.; Murugesan, V. In Situ Chemical Imaging of Solid-Electrolyte Interphase Layer Evolution in Li-S Batteries. *Chem. Mater.* **2017**, *29*, 4728–4737.
(69) Helen, M.; Reddy, M. A.; Diemant, T.; Golla-Schindler, U.; Behm, R. J.; Kaiser, U.; Fichtner, M. Single Step Transformation of Sulphur to Li2S2/Li2S in Li-S Batteries. *Sci. Rep.* **2015**, *5*, 12146.

Downloaded from pubs.acs.org/aaemcq/article-pdf/doi/10.1021/acsaem.6c02314/68937037/ae-2026-02314j.pdf by CENTRAL MICHIGAN UNIV user on 22 October 2026

https://doi.org/10.1021/acsaem.6c02314
ACS Appl. Energy Mater. XXXX, XXX, XXX–XXX